High Winds Generated by Bow Echoes. Part I: Overview of the Omaha Bow Echo 5 July 2003 Storm during BAMEX

ROGER M. WAKIMOTO

National Center for Atmospheric Research, Boulder, Colorado

HANNE V. MURPHEY AND ALBERT NESTER

Department of Atmospheric Sciences, University of California, Los Angeles, Los Angeles, California

DAVID P. JORGENSEN

National Oceanic and Atmospheric Administration/National Severe Storms Laboratory, Norman, Oklahoma

NOLAN T. ATKINS

Department of Meteorology, Lyndon State College, Lyndonville, Vermont

(Manuscript received 1 July 2005, in final form 10 January 2006)

ABSTRACT

An analysis of a bow echo that produced damaging winds exceeding F1 in intensity on the Fujita scale near Omaha, Nebraska, is shown. Part I of this study presents a combination of airborne Doppler-derived wind syntheses with a comprehensive damage survey in order to document the generation of strong winds at the surface. A detailed kinematic analysis of the evolution of a quasi-linear convective system into a bow-shaped and, subsequently, a spearhead echo is shown for the first time. It is hypothesized that a large, cyclonic bookend vortex (70–80 km in diameter) north of the bow apex enhanced the rear-inflow jet and initiated the "bowing process." A hook-shaped echo and mesovortex formed at the apex of a bowed segment of the convective line and was located to the north of the swath of strong damage rated greater than F1 in damage intensity. The peak single-Doppler radial velocity recorded by the tail radar was 43 m s^{-1} in the low-level outflow near the apex of the bow echo. The regions of the strongest single-Doppler velocities at the lowest grid level were not always associated with the most intense damage at the surface. This discrepancy may be related to the development of a stable nocturnal boundary layer that prevented the strong outflow winds from reaching the surface. An intensifying rear-inflow jet was revealed in vertical cross sections through the bow echo. The relationship between mesovortices and strong surface winds is examined in Part II.

1. Introduction

Nolen (1959) and Hamilton (1970) first noted the relationship between bow-shaped convective systems [referred to as a line-echo wave pattern (LEWP)] and straight-line damaging surface winds and tornadoes. Subsequently, Fujita (1978) documented the kinematic structure and time evolution of the radar echo of a mesoscale convective system (MCS) that he referred to as a bow echo (Fig. 1). He showed that bow echoes were frequently associated with straight-line wind damage or downbursts at the surface. Indeed, severe bow echo events can result in significant property damage and loss of life over an extended region and represent one of the more common modes of convective organization associated with severe weather (e.g., Fujita and Wakimoto 1981; Johns and Hirt 1987; Przybylinski 1995; Weisman 2001; Jorgensen and Weckwerth 2003). The MCS usually begins as a single large or small group of strong convective cells (Klimowski et al. 2004), evolves into a bow-shaped line segment, as an associated surface cold pool expands, and finally becomes a comma-shaped echo in its declining stage (Fig. 1).

Corresponding author address: Roger M. Wakimoto, NCAR/EOL, P.O. Box 3000, Boulder CO 80307.
E-mail: wakimoto@ucar.edu

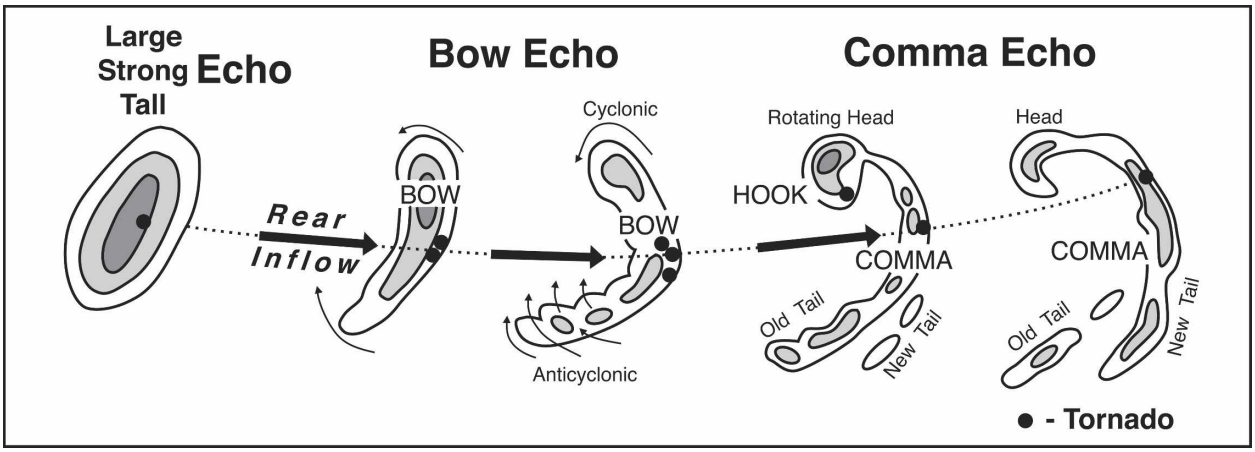

FIG. 1. Schematic diagram of the life cycle of a bow echo. Black arrows represent the approximate location of the rear-inflow jet. Black dots denote the location of tornadoes. Based on a figure from Fujita (1978).

Fujita also noted cyclonic and anticyclonic circulations at the ends of the bowing segments. Weisman (1993) referred to these counterrotating circulations as "bookend vortices."

Although bow echoes have been known to produce damaging winds at the surface for a number of years, it is surprising that there is a relative dearth of detailed observational studies that have documented these events. In particular, there are no known comprehensive studies that have captured a significant portion of the life cycle of a bow echo. Jorgensen and Smull (1993) documented a bow echo MCS and its associated northern bookend vortex using airborne Doppler radar; however, no surface damage was reported with the system (i.e., the surface winds were relatively weak). Schmidt and Cotton (1989) performed a Doppler radar analysis of a bow echo but not during the time that damaging winds were being produced. To the authors'

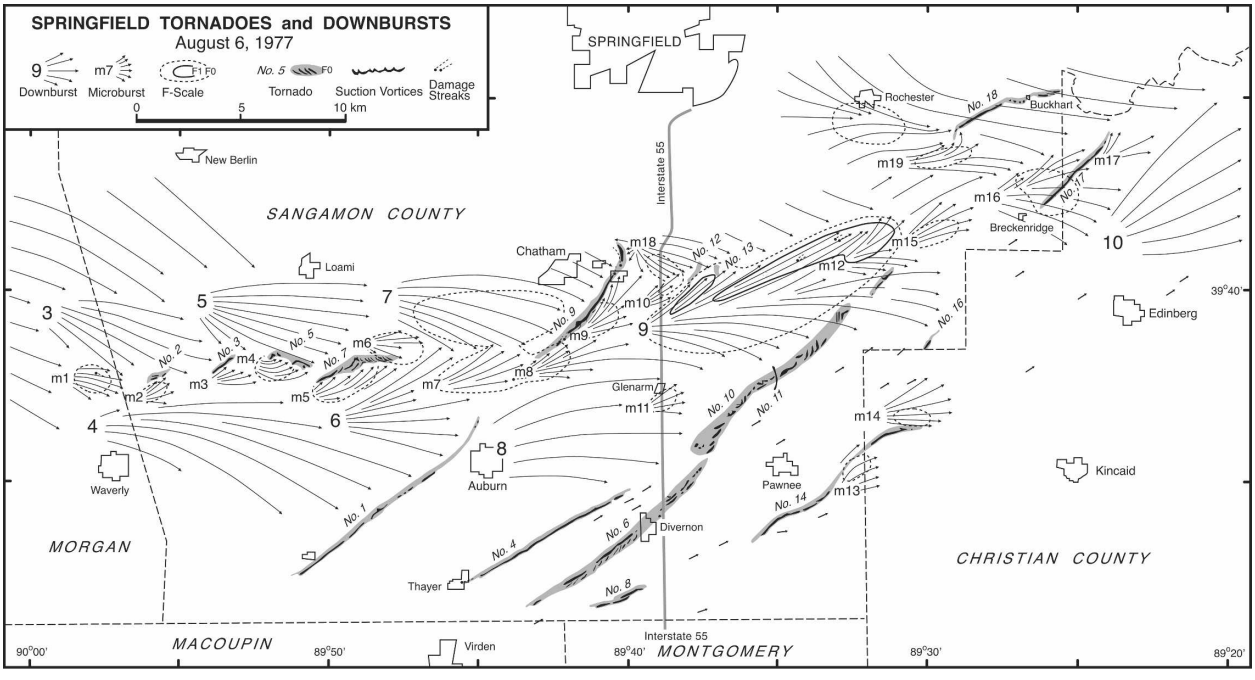

FIG. 2. Mapping of the damage from downbursts (identified by large numerals), microbursts (identified by "m"), and tornadoes (identified by "No.") on 6 Aug 1977 near Springfield, IL. Flow lines indicate the direction of damage and F-scale contours are indicated. Based on a figure from Forbes and Wakimoto (1983).

TABLE 1. ELDORA scanning mode.

Antenna rotation rate (° s^{-1})	140
No. of samples	24
PRF (Hz)	2000/2500
Gate length (m)	150
Sweep-angle beam spacing (°)	1.4
Along-track data spacing (m)	~300
Max range (km)	60
Max unambiguous velocities (±m s^{-1})	77.2
Min detectable signal at 10 km (dBZ)	~−15

TABLE 2. NOAA P-3 tail radar scanning mode.

Antenna rotation rate (° s^{-1})	60
No. of samples	32
PRF (Hz)	2133/3200
Gate length (m)	150
Sweep-angle beam spacing (°)	0.75
Along-track data spacing (m)	~1200
Max range (km)	46.8
Max unambiguous velocities (±m s^{-1})	51.5
Min detectable signal at 10 km (dBZ)	~0

knowledge, only Fujita (1979, 1981) has presented a multi-Doppler radar study of a severe bow echo while it produced destructive winds and a tornado; however, it was only for one analysis time and was confined to a single height. There have been a number of studies that have used single-Doppler radar to examine bow echoes and their relationship to damaging winds at the surface (e.g., Burgess and Smull 1990; Przybylinski 1995; Atkins et al. 2004).

Bow echoes are associated with a storm-relative rear-inflow jet and rear-inflow notch (Fujita 1978; Smull and Houze 1987; Schmidt and Cotton 1989; Jorgensen and Smull 1993; Przybylinski 1995). The jet with its core at the apex of the bow is associated with the bulging and acceleration of the radar echoes. Chong et al. (1987), Weisman (1992), Lafore and Moncrieff (1989), Lin and Johnson (1994), and Klimowski (1994) have shown that the rear inflow is largely driven by processes occurring within the MCS.

The prevailing hypothesis has been that the descending rear-inflow jet, upon reaching the surface, was primarily responsible for the damaging winds (e.g., Burgess and Smull 1990; Weisman 1993; Przybylinski 1995). Indeed, extensive aerial and ground surveys of damage in the aftermath of bow echoes revealed large regions of destruction that could be attributed to a descending rear-inflow jet (e.g., Fujita 1978). Embedded within these extensive areas of damage, however, were pockets or swaths of more extreme or concentrated destruction that occurred on a much smaller scale, as shown by Forbes and Wakimoto (1983). A detailed damage map from their study is shown in Fig. 2. The damage was attributed to 10 downbursts and 19 microbursts, with the latter often in close proximity to a number of the tornado tracks. These smaller-scale damage patterns could not be readily attributed to the descending rear-inflow jet. Other damage surveys presented by Fujita (1978, 1981), Fujita and Wakimoto (1981), and Funk et al. (1999) supported the results shown in Fig. 2. The existence of two scales of downdrafts within MCSs was first noted by Zipser (1977) and Houze (1977).

Wakimoto (2001) hypothesized that these small swaths might be associated with the convective-scale downdrafts (i.e., microbursts) produced by thunderstorms within the leading convective line [also suggested by Fujita (1978) and Burgess and Smull (1990)]. In contrast, Weisman and Trapp (2003) and Trapp and Weisman (2003) hypothesized, based on numerical simulations, that damage often attributed to microbursts was induced by strong low-level mesovortices. The intense low-level winds appeared to be accelerated by the large horizontal pressure gradients generated by these mesovortices rather than by intense downdrafts. This close relationship between straight-line winds and intense mesovortices is supported by the survey presented in Fig. 2. Note that several tornadoes

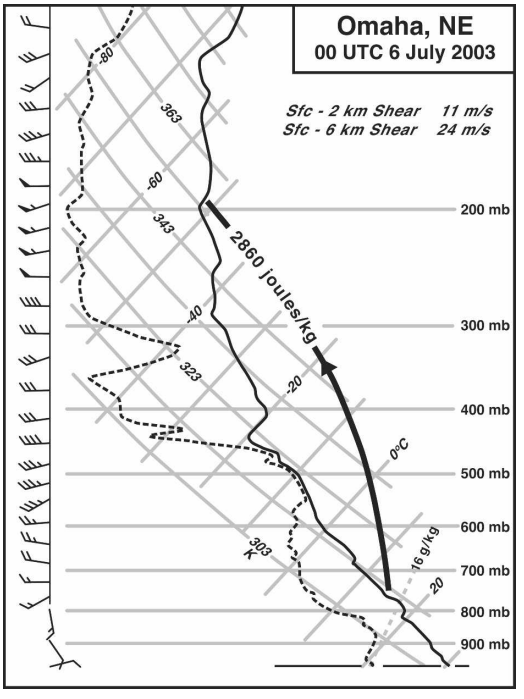

FIG. 3. Thermodynamic sounding launched from Omaha at 2300 UTC 5 Jul 2003. The thick, black line represents the path of a displaced parcel from the surface. Wind vectors are plotted with the flag, full barb, and half-barb representing 25, 5, and 2.5 m s^{-1}, respectively.

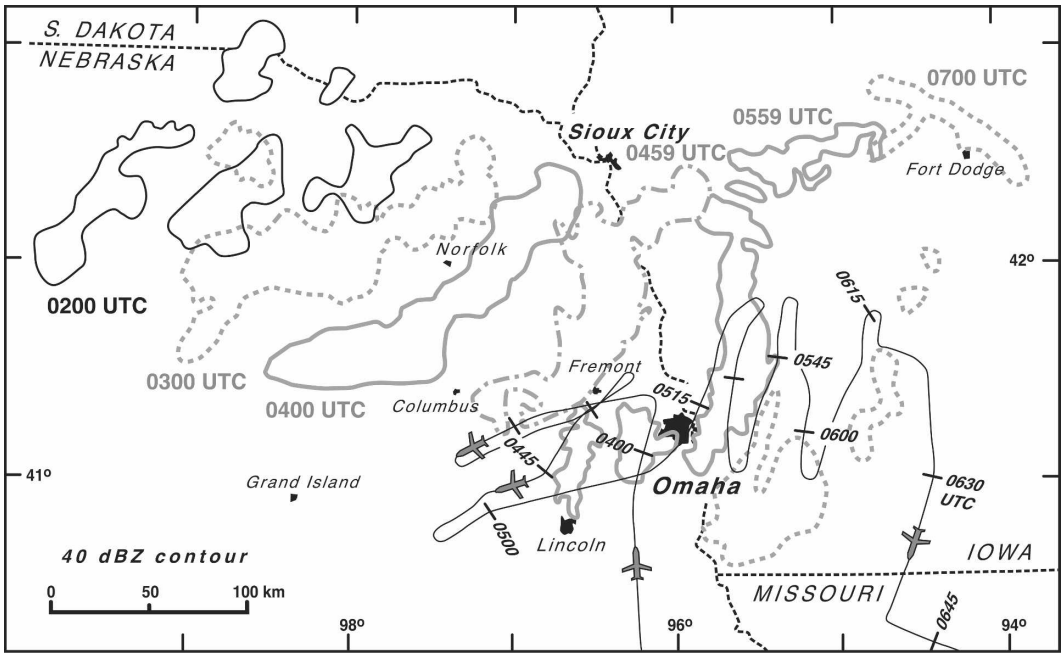

FIG. 4. Isochrone analysis of the Omaha bow echo. The 40-dB*Z* contour is drawn at 1-h intervals. Different line types are drawn in order to distinguish the echo at the various times. The flight track of the NRL P-3 is shown.

in the figure are accompanied by microburst damage immediately to the south of the track.

A squall line developed over eastern Nebraska in the evening of 5 July 2003 during the Bow Echo and Mesoscale Convective Vortex (MCV) Experiment (BAMEX; Davis et al. 2004) and was observed by two Doppler radar–equipped turboprop aircraft from ~0430 to 0800 UTC. One of the goals of the experiment was to sample bow echo systems that are associated with damaging winds at the surface. The radar echo associated with the line assumed a bow shape near Omaha, Nebraska (OAX), during the time that numerous high wind reports were received by the National Weather Service (NWS). High-resolution Doppler radar measurements were made of the bow echo while it was creating damage rated F1 in intensity (Fujita 1981). Part I of this study presents the overall evolution of the 5 July storm (hereafter, referred to as the Omaha bow echo). High-spatial-resolution Doppler analyses of a quasi-linear convective system that subsequently assumes a bow shape and its relationship with the overall surface damage are documented. This is the first time that such an analysis has been presented. A mesovortex and accompanying hook-shaped echo appendage developed near the apex of a segment of the line that assumed a bow shape. A large region of intense surface damage was documented at the apex during the time that the vertical vorticity associated with the mesovortex was the strongest. The second part of the study provides a detailed analysis of the mesovortices that were resolved in the Doppler wind syntheses and their relationship to intense damage swaths at the surface.

Section 2 discusses BAMEX and the airborne Doppler radars deployed during the experiment. The environmental conditions, storm evolution, and damage survey are shown in section 3. Section 4 presents single- and multi-Doppler radar analyses of the bow echo. A summary and discussion is presented in section 5.

2. BAMEX and the airborne Doppler radars

a. BAMEX

The field phase of BAMEX took place in spring and summer of 2003 and was based at MidAmerica St. Louis Airport in Mascoutah, Illinois (near St. Louis, Missouri). The objective of the experiment was to sample the multiscale aspects of two types of MCSs throughout a majority of their life cycles (Davis et al. 2004). One type of MCS was the bow echo systems that are associated with damaging winds at the surface, and the other type was those systems that produced long-lived MCVs. The experiment relied on the deployment of mobile ground-based and airborne observing platforms because MCSs can develop over an extended region and travel over large distances (e.g., Laing and Fritsch 1997). Unfortunately, the ground-based platforms were unable to intercept the 5–6 July Omaha

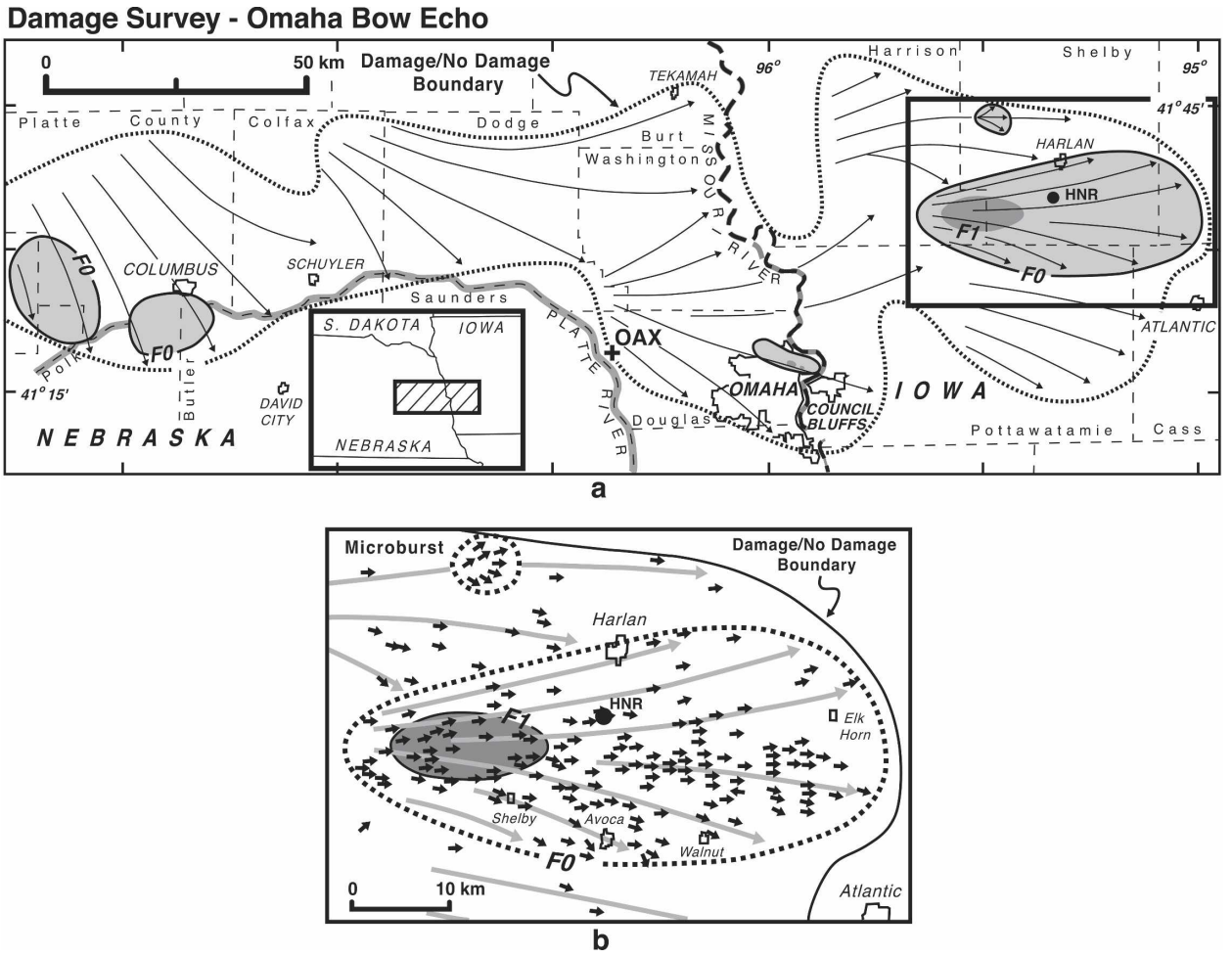

FIG. 5. Map of the surface damage produced by the Omaha bow echo. The map was compiled based on several days of aerial and ground surveys throughout the region. (a) The location of the map is indicated by the hatched box in the inset. (b) An enlargement of the boxed-in region on the east side of (a) is shown. The flow lines represent the direction of fallen trees or structural damage. The outer extent of the damage as well as the regions rated F0 and F1 in damage intensity are indicated in the figures. The black arrows in (b) represent individual vectors of damage to trees or structures. The black dot in (a) and (b) denotes the location of the HNR automated surface station.

bow echo so the following analysis is centered on the capabilities of the aircraft.

b. ELDORA

The National Center for Atmospheric Research (NCAR) maintains and operates a 3-cm airborne Doppler radar [Electra Doppler Radar (ELDORA)]. ELDORA is equipped with two back-to-back antennas mounted within the tail section of a Naval Research Laboratory (NRL) P-3 aircraft. The antennas scan vertically and the beams are directed slightly fore and aft of normal to the fuselage of the aircraft by ~18.5°. The antenna scan pattern is conical as the aircraft moves forward. ELDORA uses a multiple-beam scanning technique, which is a variation of the fore–aft scanning technique (FAST; Jorgensen et al. 1996), in order to collect data that can be used in a dual-Doppler wind synthesis. A list of ELDORA's scanning parameters during BAMEX is shown in Table 1. For more information regarding ELDORA's hardware and design, the interested reader is referred to Hildebrand et al. (1994, 1996).

A principal limitation of an airborne Doppler radar is its along-track data or beam-intersecting spacing, which is a function of the antenna rotation rate and aircraft ground speed. The fore and aft beams intersected with a spacing of ~300 m for ELDORA. Another limitation is the time lag between intersecting fore and aft beams. For a typical aircraft ground speed of ~120 m s^{-1}, the time lag is ~1 min (10 km)$^{-1}$ of

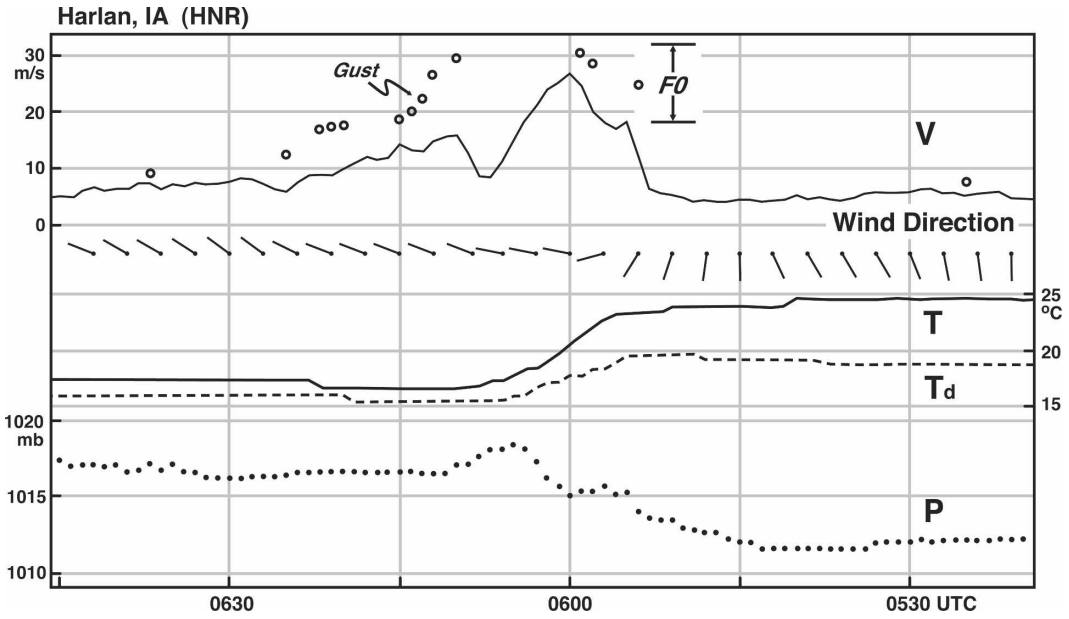

FIG. 6. Time series of mean wind speed and direction, temperature, dewpoint temperature, and pressure from the HNR automated surface station. The peak gusts are shown by the open circles. Wind speed and direction are 2-min running averages based on data collected every second. The peak gust is the highest 5-s-averaged wind speed for the preceding 10 min. The range of wind speeds associated with F0 damage intensity is shown on the figure. The location of the station is shown in Fig. 5.

range. For example, if the leading convective line were ~15 km from the aircraft, the time lag would be 90 s. Stationarity of the processes must be assumed during this lag. This is not an uncommon assumption in dual-Doppler analyses.

The flight plan for the NRL P-3 was to fly relatively straight and level racetrack patterns at low levels [~1.6 km above ground level (AGL); hereafter, all heights are AGL]. The tracks were long (~100 km) and flown generally within 10–15 km ahead of the leading edge of the convective line. The flight pattern required the aircraft to fly along and parallel to the advancing gust front (the front was often positioned as close as 2–3 km from the aircraft). These tracks were a challenge to execute owing to the nonlinear nature of many of the boundaries and the possibility that the gust front could "surge out" ahead of the bow echo in response to strong outflow winds. Accordingly, the mission scientist was required to make continuous corrections to the aircraft heading in flight.

The main advantage of the NRL P-3 flight track was the ability to resolve the detailed kinematic structure of the bow echo over an extended path with its ELDORA radar. The main disadvantage was the time required to execute one leg (12–13 min), which decreased the temporal resolution (time required to complete a subsequent leg). The uniqueness of the dataset collected by flying extended legs far outweighed the degradation of the temporal resolution for the analyses presented here.

There were two reasons that justified the NRL P-3's position out ahead of the storm system. First, ELDORA is capable of detecting echoes and Doppler velocities within the "clear air" (Wakimoto et al. 1996). This capability was critical because the gust front could be devoid of precipitation scatterers. Second, the along-track resolution of ELDORA was sufficient to resolve mesovortices forming along the gust front if they were present.

c. NOAA P-3

The National Oceanic and Atmospheric Administration (NOAA) operates a P-3 that is equipped with an airborne Doppler radar (Jorgensen et al. 1983). This airborne radar also uses FAST, which allows for the collection of Doppler velocity data that can be synthesized into a wind field. However, the along-track data spacing is greater than that for ELDORA owing to the relatively slow antenna scan rate (see Table 2) and the lack of a second transmitter to simultaneously collect fore and aft beams. The sensitivity of the NOAA P-3 Doppler radar is also less than that of ELDORA (Table 2); accordingly, it cannot detect many clear-air echoes.

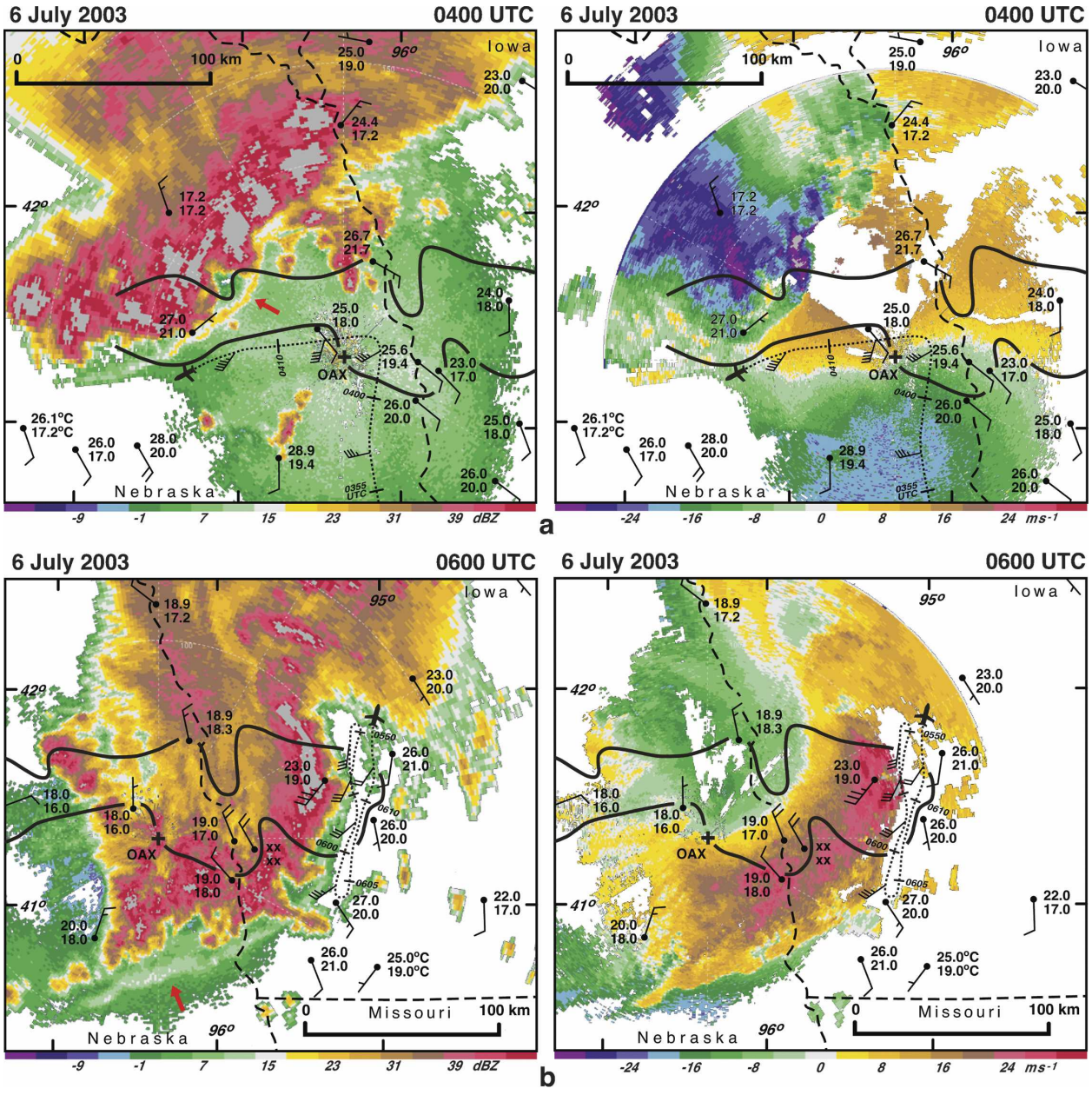

FIG. 7. Radar reflectivity and single-Doppler velocity from the OAX WSR-88D at (a) 0400 and (b) 0600 UTC. The black line represents the extent of the damage reported at the surface based on the analysis presented in Fig. 5a. The dotted line represents the flight track of the NRL P-3. The flight-level winds are shown along the track. Surface reports of temperature, dewpoint temperature (°C), and wind speed and direction are plotted. The location of the radar is shown by the black cross. Wind vectors are plotted with the full barb and half-barb representing 5 and 2.5 m s^{-1}, respectively. The thick, dashed lines are the state borders. The gray color in radar reflectivity and Doppler velocity represents values that are off the scale. The red arrows on the radar reflectivity plot denote the position of a thin line.

The decreased along-track resolution and sensitivity of the radar suggested that the NOAA P-3 aircraft should fly to the rear of the convective line and within the trailing stratiform region to map the rear inflow and any bookend vortices that may be present (Davis et al. 2004, see their Fig. 2a). In addition, the two aircraft attempted to synchronize their flight tracks during missions so that radar data could be nearly simultaneously collected in the domain between the aircraft such that a "quad-Doppler" synthesis (Hildebrand et al. 1996; Jorgensen et al. 1996) could be performed. The quad-Doppler technique reduces the uncertainty of the de-

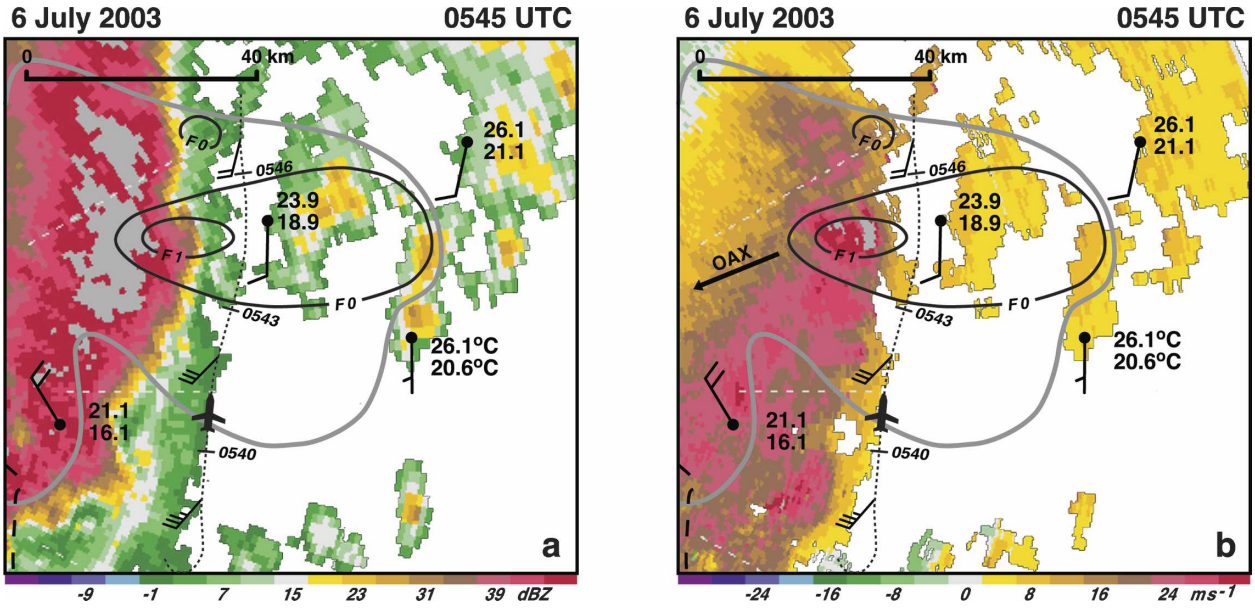

FIG. 8. (a) Radar reflectivity and (b) single-Doppler velocity from the OAX WSR-88D at 0545 UTC. The dotted line represents the flight track of the NRL P-3. The flight-level winds are shown along the track. The gray and black lines are based on the damage map shown in Fig. 5a. Surface reports of temperature, dewpoint temperature (°C), and wind speed and direction are plotted. The azimuthal direction to the OAX radar is shown by the black arrow in (b). Wind vectors are plotted with the full barb and half-barb representing 5 and 2.5 m s^{-1}, respectively. The gray color in radar reflectivity and Doppler velocity represents values that are off the scale.

rived vertical velocities in the region of overlapping coverage.

3. Environmental conditions, storm movement, and the damage survey

There was an extensive region of large convective available potential energy (CAPE) from 1500 to 3000 J kg^{-1} over large sections of Nebraska, Iowa, Missouri, and Illinois by the early evening of 5 July (not shown). Southerly flow at the 850-mb level was advecting warm, moist air into Kansas and Nebraska, and an upper-level shortwave trough was propagating through South Dakota and Nebraska (not shown). A sounding that was representative of the environmental conditions was launched from Omaha at 0000 UTC 6 July (Fig. 3). The CAPE was estimated to be 2860 J kg^{-1} and the surface to 6 km integrated shear was ~24 m s^{-1}, within the range of values that could support bow echoes (e.g., Evans and Doswell 2001; Coniglio et al. 2004). A dropsonde released ~90 km southeast of Omaha at 0202 UTC (not shown) exhibited a similar wind shear. The thermodynamic profile was also consistent, except for several degrees of surface nocturnal cooling and a 1°–2°C warming in the 800–500-mb layer. The CAPE for this sounding was estimated to be ~1600 J kg^{-1}.

Scattered thunderstorms initiated over southwestern South Dakota by ~1900 UTC 5 July. The storms moved southeastward into north-central Nebraska by 0100 UTC and slowly organized into a quasi-linear convective system. An isochrone analysis of the radar reflectivity pattern associated with the storm during the period from 0200 to 0700 UTC is shown in Fig. 4. The echoes associated with the MCS assumed a bow shape at ~0400 UTC based on time-lapse images of the radar reflectivity from the OAX Weather Surveillance Radar-1988 Doppler (WSR-88D) data. The echo maintained a convex shape for several hours until there was rapid dissipation of the storm complex around 0700.

Also plotted in Fig. 4 is the flight track of the NRL P-3. The aircraft first intercepted the bow echo at ~0405 UTC and began flying a series of southwest–northeast legs. Convection that developed ahead of the bow echo prevented the aircraft from flying further to the north at this time. This convection soon dissipated and by 0500 UTC the P-3 was able to execute five north–south flight legs centered on the apex of the bow echo.

The strong winds accompanying the bow echo led to widespread reports of damage in eastern Nebraska and western Iowa (NCDC 2003). Numerous trees were blown down and a number of structures were damaged. A detailed aerial and ground survey was undertaken several days after this event in order to document the extent of the damage. Two light aircraft flew over the

affected area on two consecutive days. Ground surveys of the region were also performed over a 2.5-day period. The results of the surveys are presented in Fig. 5. The direction of each fallen tree and large limb in the affected area was plotted. Damage intensity was determined by the number and size of downed trees in a particular region. The dotted line in Fig. 5 represents the region beyond which no damage was documented. There were several areas rated greater than F0 in damage intensity on the Fujita scale (Fujita 1981). The area between the dotted line and the F0 contour was characterized by sporadic damage (e.g., large limbs broken off and an occasional tree down). The alignment of the damage vectors is shown by the flow lines, but it was subjectively assessed as not meeting the F0 criteria owing to the lack of continuous damage in the region. There was a significant area of damage rated greater than F1 located ~20 km southwest of Harlan, Iowa (HNR), and two isolated pockets of damage rated F1 in northern Omaha. The documentation of the surface damage in the aftermath of the Omaha bow echo is important because it represents the "ground truth" when compared to the wind syntheses of the Doppler radar data to be shown later.

The Omaha bow echo created an east–west swath of damage in eastern Nebraska and western Iowa that was ~50 km wide and over 200 km long. These dimensions are comparable to the well-documented northern Wisconsin damage survey performed by Fujita (1978). It is also consistent with other cases shown by Fujita (1978, 1981), Fujita and Wakimoto (1981), and Forbes and Wakimoto (1983). The flow arrows suggest that the damaging winds were from the northwest near Columbus, Nebraska. The damaging winds slowly shift and are from a westerly direction near the Missouri River into western Iowa (Fig. 5a). No tornado tracks were documented during the survey owing to the absence of any linear damage tracks or circulation patterns in the downed trees (see Fujita 1981; Forbes and Wakimoto 1983). The relative absence of damage immediately to the east of the Missouri River does not appear to be related to topography. Instead, it appears to be a result of a temporary weakening of the near-surface winds followed by a reintensification of the descending rear-inflow jet and the development of a bow echo apex that is documented in section 4.

An enlargement of the area experiencing the greatest damage in western Iowa is enlarged in Fig. 5b. The individual vectors of fallen trees/limbs and structural damage are shown. The characteristic diffluent pattern (as shown by the gray arrows, see also Fujita 1981) is evident in the region rated >F0 in damage intensity.

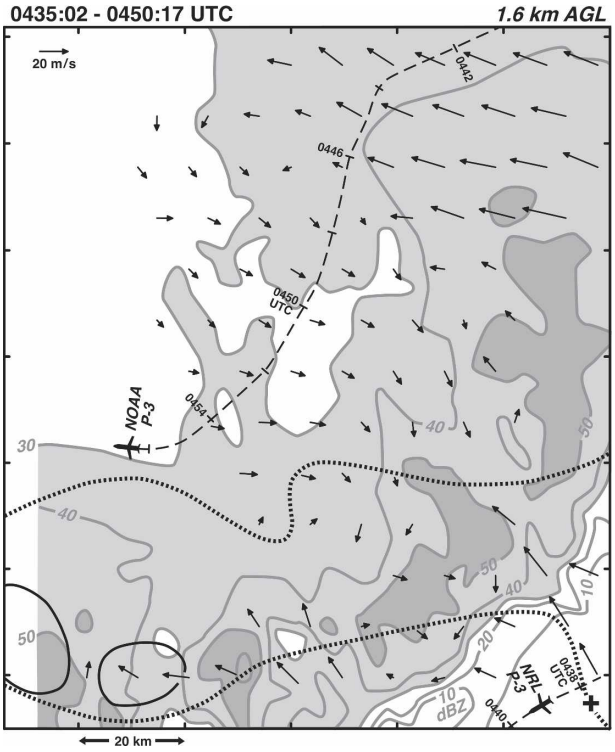

FIG. 9. Multi-Doppler wind synthesis that combines radar data recorded by the NOAA P-3 and NRL P-3 at 0435:02–0450:17 UTC at 1.6 km AGL. Storm-relative winds are plotted. The radar reflectivity is from the WSR-88D located at Omaha (position indicated by the black cross). Gray lines are radar reflectivity with values >30 dBZ shaded light gray and >50 dBZ shaded dark gray. Aircraft tracks are depicted by the thin dashed lines. The damage at the surface is based on the results presented in Fig. 5a and is shown by the dotted and solid black lines.

There was also a pronounced microburst pattern in the damage ~15 km northwest of Harlan. Fortunately, there was an automated weather station located near HNR and within the F0 region. The time series of data reveals that the surface wind direction shifts from southerly to westerly after the passage of the gust front (Fig. 6). The temperature and dewpoint temperature both show a characteristic drop and the pressure rose. The mean wind speed and peak gust increased within the cold air. The range of wind speeds that are associated with F0 in damage intensity is indicated in Fig. 6. Unfortunately, there were several time intervals when no peak gusts were recorded at the HNR station. The values that are plotted, however, all lie within the F0 range. This is consistent with the aerial and ground survey, which rated the damage in this region between F0 and F1. It should be noted that the survey shown in Fig. 5 was finalized before examining the HNR wind data. Hence, the latter provided an independent check of the estimated damage intensity scale even though

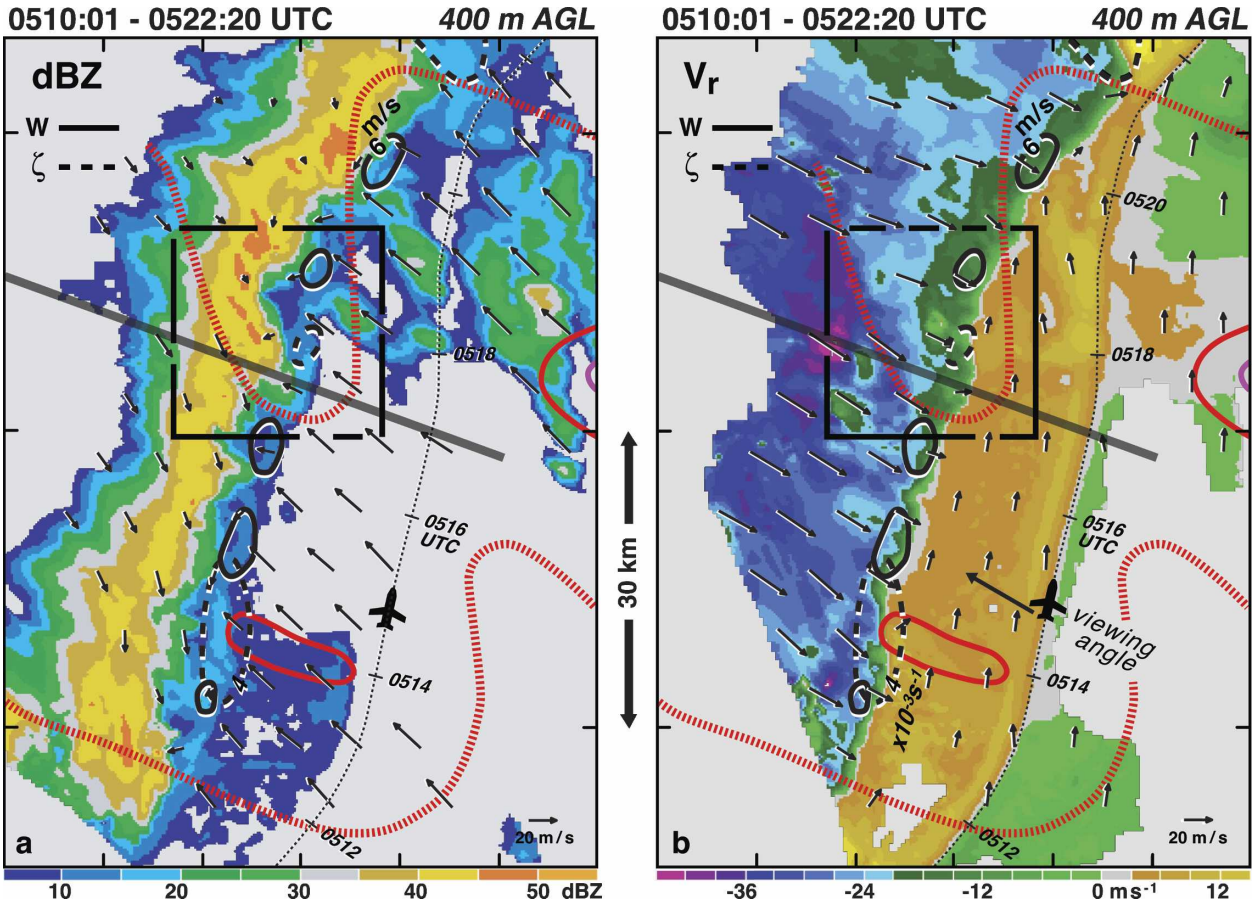

FIG. 10. Dual-Doppler wind synthesis at 0510:01–0522:20 UTC at 400 m AGL. (a) Storm-relative winds superimposed onto radar reflectivity and (b) ground-relative winds superimposed onto single-Doppler velocities. Vertical vorticity (dashed lines) and velocity (solid black lines) are plotted on both figures. The dotted line represents the flight track of the NRL P-3. The damage at the surface is based on the results presented in Fig. 5a and is shown by the dashed red, solid red, and magenta lines. The black box is enlarged in Part II. The gray line indicates the position of a vertical cross section shown in Fig. 11. The viewing angle of the radar is shown in (b).

such comparisons should be viewed with caution (Doswell and Burgess 1988).

4. Radar analyses

a. Single-Doppler analyses

The radar reflectivity and single-Doppler velocity data from the OAX WSR-88D at 0400 and 0600 UTC are shown in Fig. 7. Also plotted on the figure are the surface weather data and damage/no-damage boundary based on the results presented in Fig. 5. Surface temperatures were a few degrees colder than the values shown in the sounding launched from Omaha (Fig. 3), suggesting that the environmental air at low levels had stabilized. Accordingly, the comparison of single-Doppler velocities with the damage survey illustrated in this figure is important. It is possible that the high winds measured by the radar at the lowest elevation angle remained aloft and may not be reaching the surface owing to the ambient stratification.

A gust front was apparent as a thin line of radar reflectivity and as a gradient of Doppler velocities (Wilson and Schreiber 1986). The winds behind the front at 0400 UTC were strong with magnitudes >40 m s^{-1} (Fig. 7a). Note that there is no obvious relationship between the regions of high Doppler velocities and the damage reported at the surface. This may, in part, be due to the height of the center of the beam above the ground ($\sim$1 km) at long ranges from the radar location. The NRL P-3 flight track is also plotted on Fig. 7 and illustrates that several flight legs were flown close to the apex of a bowing segment of the convective line (Fig. 7b). An enlargement of the bow apex at 0545 UTC, when the winds were producing an extensive area of damage rated greater than F1 in intensity, is shown in

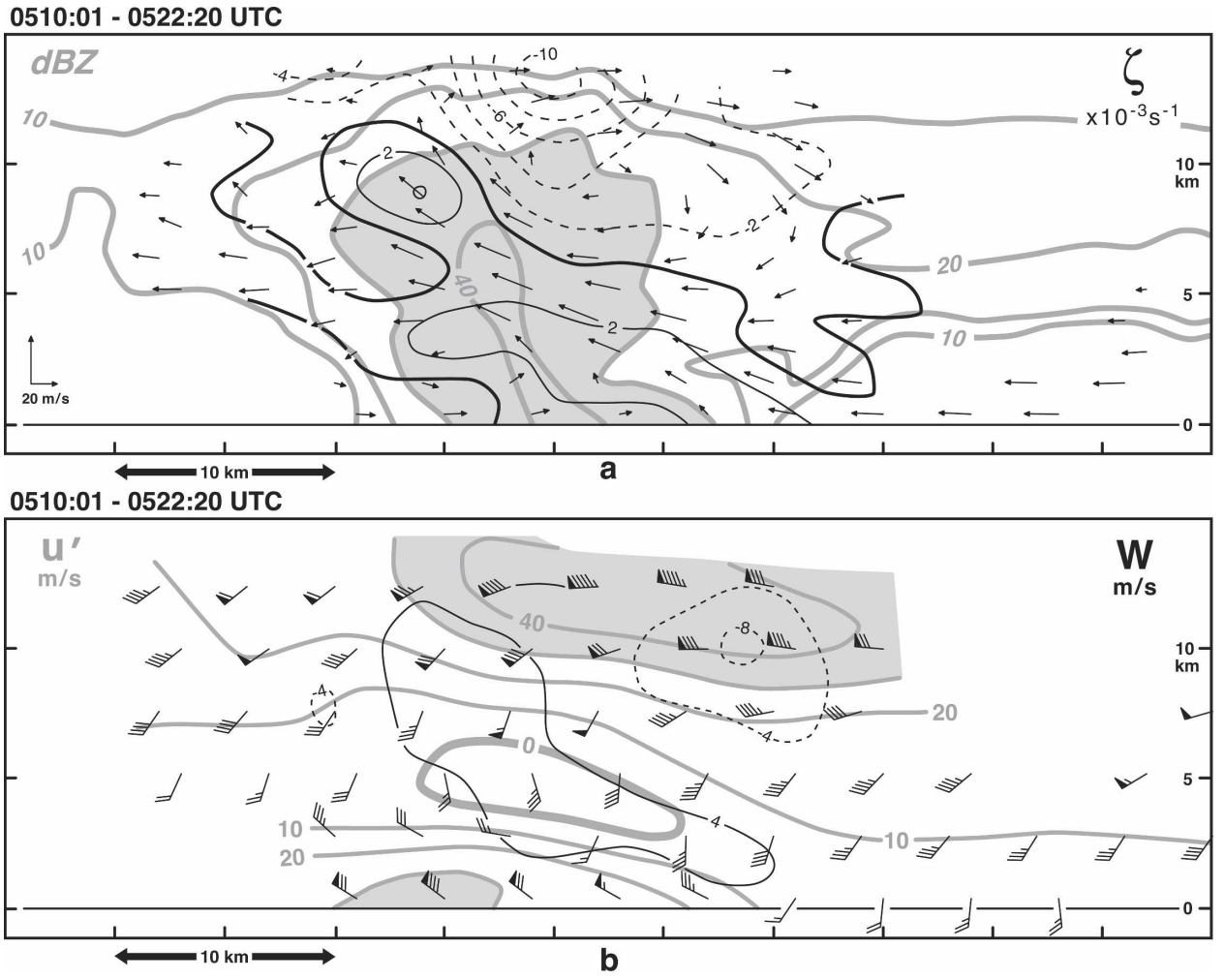

FIG. 11. Vertical cross section through the developing apex at 0510:01–0522:20 UTC. (a) Radar reflectivity, vertical vorticity, and storm-relative winds vectors in the plane of the cross section. (b) Vertical velocity, total horizontal velocity vector, and component of ground-relative flow in the plane of the cross section. Radar reflectivities and ground-relative flow greater than 30 dBZ and 30 m s^{-1}, respectively, are shaded gray. Horizontal velocity vectors are plotted with the flag, full barb, and half-barb representing 25, 5, and 2.5 m s^{-1}, respectively. Location of the cross section is shown in Fig. 10.

Fig. 8. The strongest Doppler velocities away from the radar were near the apex and confined within the region outlined by the F1 isopleth. This is an example of the good agreement between the measured wind speeds and the damage survey.

b. Multi-Doppler analyses

As previously mentioned, there were a total of five ELDORA legs flown along the leading edge of the convective region. Two additional wind syntheses were created by merging the data collected by ELDORA and the NOAA P-3 radar. Fortunately, these data captured the evolution of the MCS from a quasi-linear convective system to a bow echo. The comparison of the Doppler analysis with the damage survey facilitates the understanding of where the strongest low-level winds are generated. The details of the wind syntheses are presented in the appendix.

1) 0435:02–0450:17 UTC

An analysis of the dual-Doppler wind synthesis that combines the data collected by ELDORA and the NOAA P-3 radar from 0435 to 0450 UTC at 1.6 km is shown in Fig. 9. The relatively coarse resolution of this Doppler analysis provided an opportunity to import the reflectivity data from the nearby WSR-88D radar located at Omaha in order to minimize the effects of attenuation suffered by the airborne radars. As stated in the appendix, the imposed filtering on the wind field effectively removes smaller-scale features (e.g., meso-

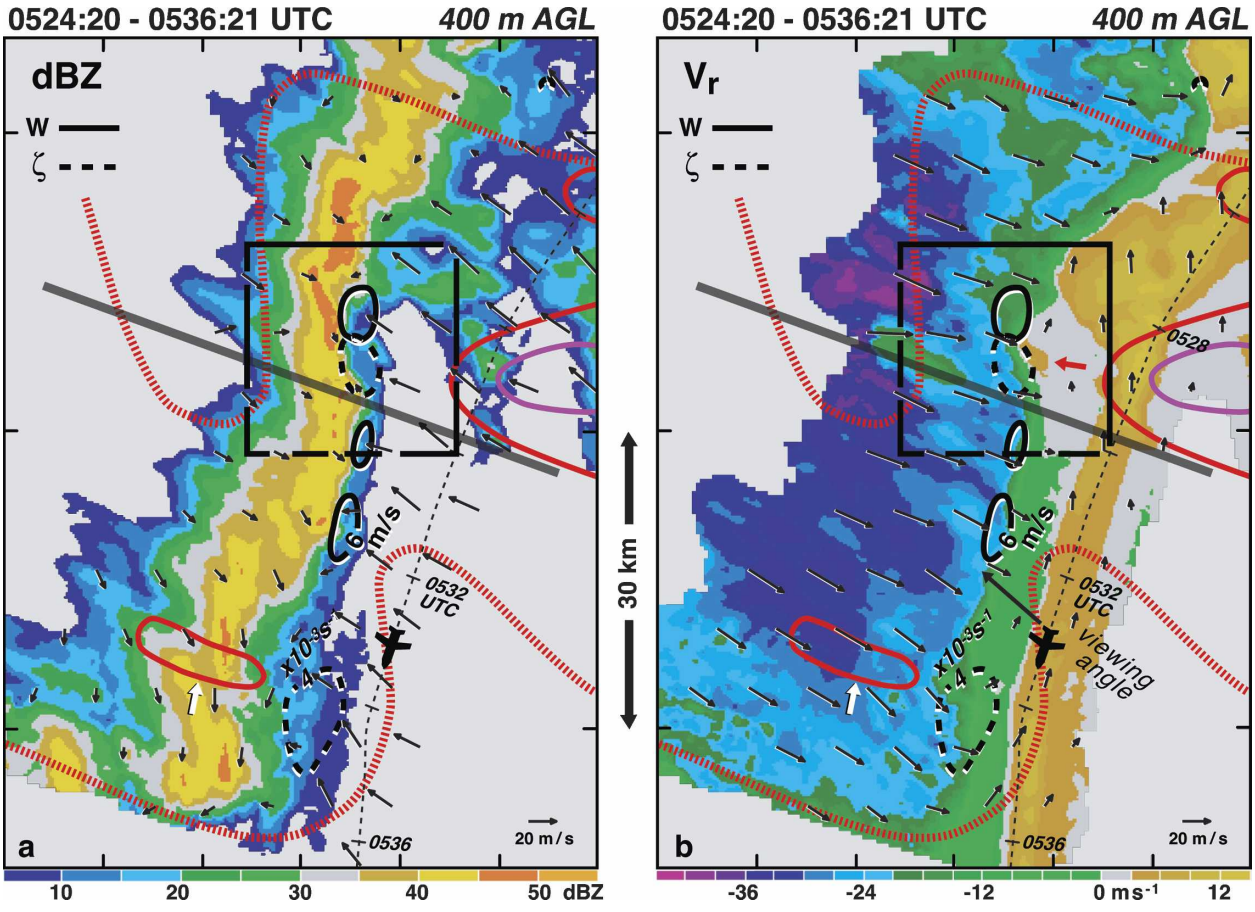

FIG. 12. Same as Fig. 10, but for 0524:20–0536:21 UTC at 400 m AGL. The gray line indicates the position of a vertical cross section shown in Fig. 13. Red arrow in (b) indicates the position of a developing rotational couplet in single-Doppler velocity. The white arrow indicates the location of the F0 contour in northern Omaha.

vortices). As a result, only the system-scale circulations are resolved.

A rear-inflow jet (10–15 m s^{-1}) centered within the rear-inflow notch is shown. The ground-relative strength of this jet was 30–35 m s^{-1} and is seen extending toward the bow apex and the damage reported at the surface. The damage covered a large region at this time but was rated <F0. A shear zone is evident along the northeastern edge of the rear inflow; however, no closed circulation is readily apparent in the wind field. Accordingly, this period may best be described as the incipient stages of the cyclonic bookend vortex. The two aircraft were too far apart at this time to construct a true quad-Doppler wind synthesis of the convective line because there was little overlap of the analysis domains.

2) 0510:01–0522:20 UTC

The first ELDORA-only pass along the leading edge of the line of intense convection is shown in Fig. 10. The storm was approaching the western suburbs of Omaha at this time (refer to Fig. 5) and the outflow winds were causing minor damage in the countryside. Single-Doppler velocities toward the radar in the postfrontal air were >40 m s^{-1}. The viewing angle of the antenna was fortuitous because it was nearly parallel to the postfrontal wind field shown in Fig. 10b. Therefore, the single-Doppler velocities approximate the full component of the wind.

Both the storm- (Fig. 10a) and ground- (Fig. 10b) relative winds are presented because the latter is responsible for the damage presented in Fig. 5. The convection was quasi linear at this time and there was a shift from southerly to northwesterly winds across the gust front (Fig. 10b), consistent with the time series shown in Fig. 6. The position of the gust front is shown by the boundary between the negative and positive single-Doppler velocities located ~10 km to the west of the flight track (Fig. 10b). Updrafts along the gust front were >6 m s^{-1}, and there were several regions where

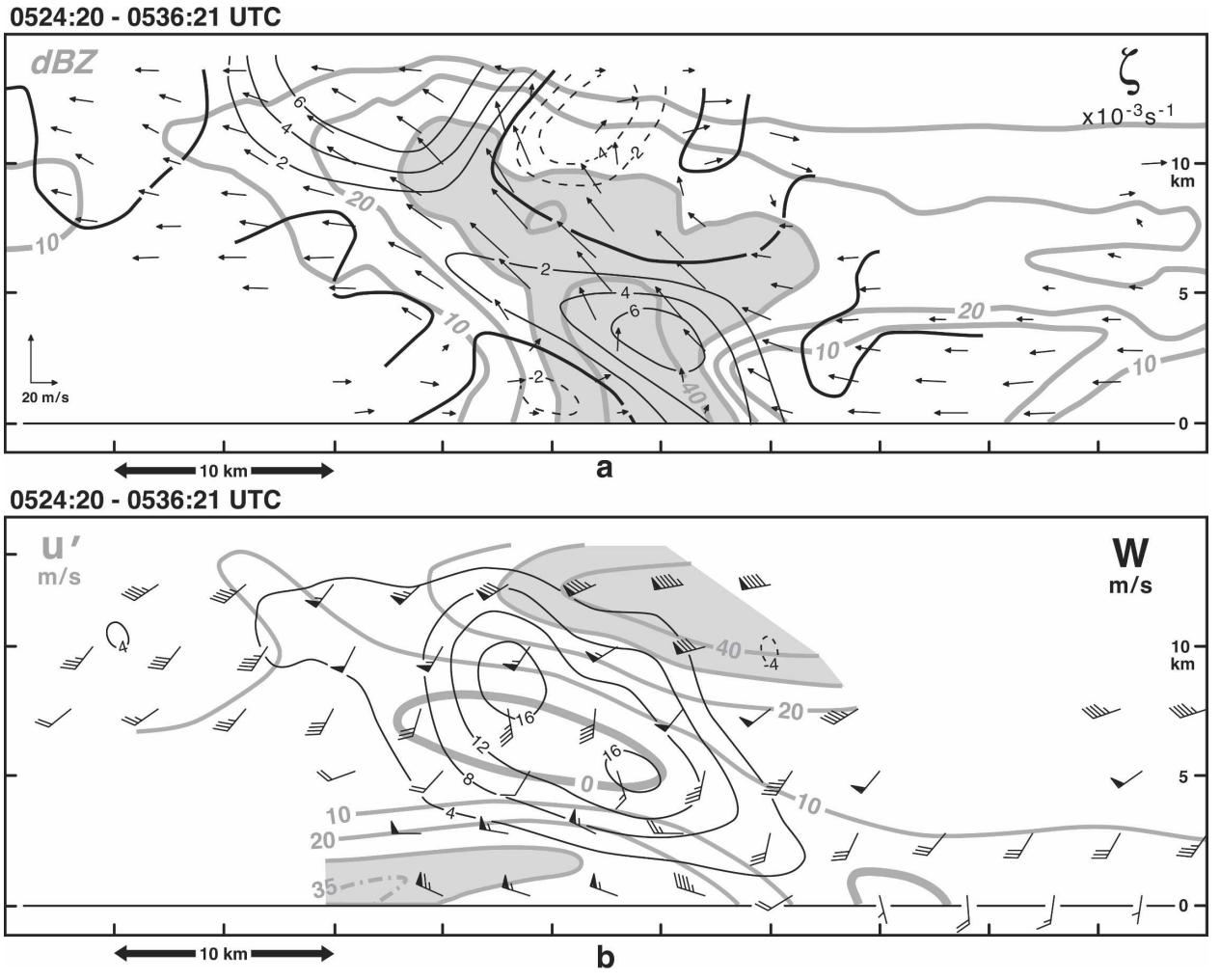

FIG. 13. Same as Fig. 11, but for 0524:20–0536:21 UTC. Location of the cross section is shown in Fig. 12.

the vertical vorticity was $>4 \times 10^{-3}$ s^{-1}. It should be noted that a comparison of the echo patterns shown in Figs. 7 and 10 illustrates the importance of attenuation that is common when scanning a severe storm with an X-band aircraft radar (e.g., Hildebrand et al. 1981). Fortunately, Doppler velocities were not as severely impacted and were typically recorded at a greater range from the radar.

An approximate west–east vertical cross section was produced in the region where the apex of the bow echo would subsequently develop (Fig. 11). The classical model of the flow within a squall line associated with a trailing stratiform region is apparent (e.g., Houze et al. 1989). A layer of upward-sloping, front-to-rear flow atop a rear-inflow jet is evident in Fig. 11. There was weak cyclonic vorticity at the interface between these two flows (Fig. 11a) and the updrafts were >4 m s^{-1}. The ground-relative winds at low levels were $\sim$40 m s^{-1} from the north-northwest, and the component in the plane of the cross section was >30 m s^{-1} (Fig. 11b). The kinematic depth of the outflow was $\sim$3 km.

3) 0524:20–0536:21 UTC

A segment of the convective line, $\sim$30 km in length, has begun to "bow out" based on the data collected during the southerly pass by the aircraft. The formation of a bow at this time agrees with the increase in damage reported east of the Missouri River as indicated by the damage contours superimposed onto the analysis (Fig. 12). This was also the time when F0 and F1 damage was occurring in northeast Omaha (indicated by the white arrow). There is a region of cyclonic vorticity $>4 \times 10^{-3}$ s^{-1} located east of the F0 damage contour. This cyclonic vorticity was also apparent but was located further to the west in the earlier analysis time (Fig. 10a). This vorticity feature appears to support the hy-

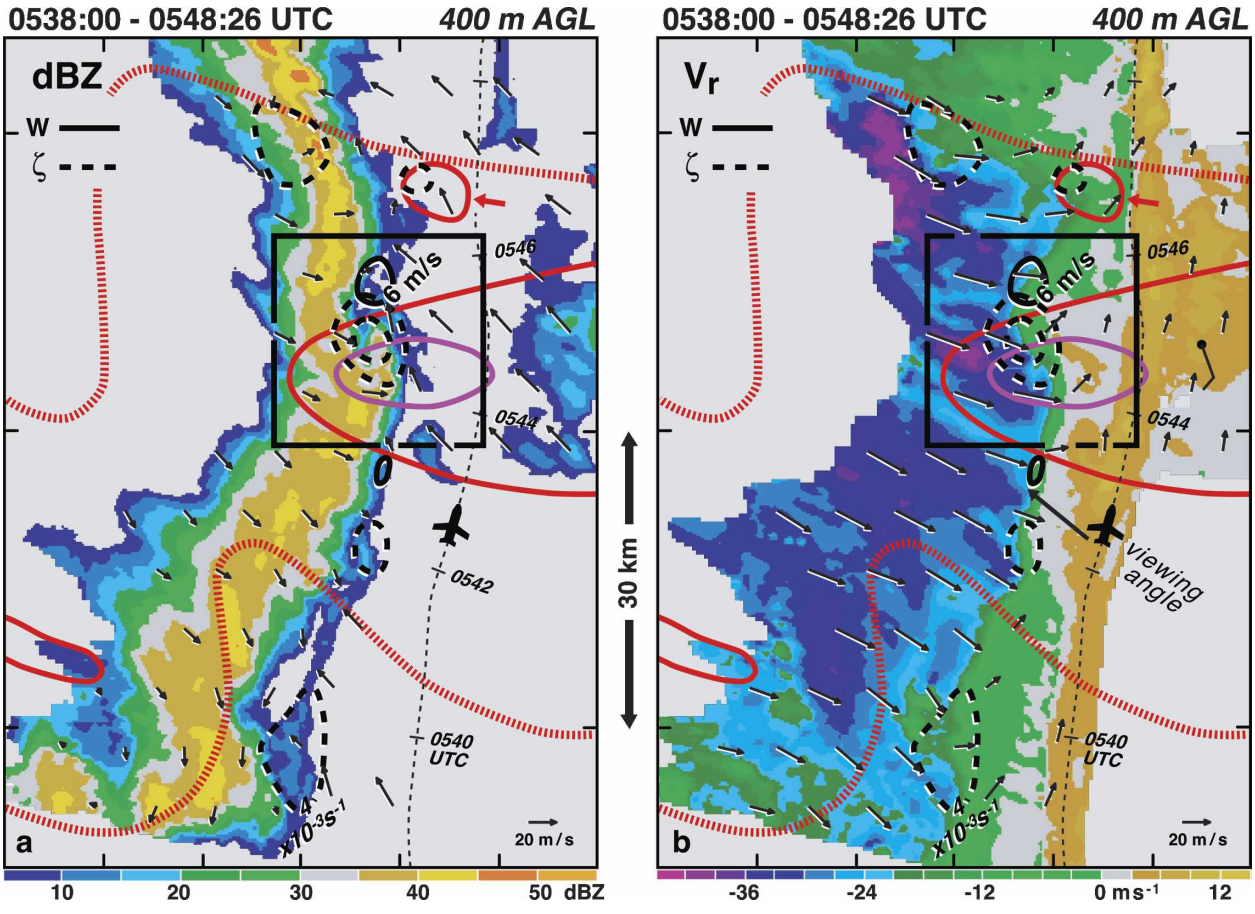

FIG. 14. Same as Fig. 10, but for 0538:00–0548:26 UTC at 400 m AGL. Surface wind report from HNR is shown on the single-Doppler velocity plot. Red arrow denotes the F0 contour associated with a microburst.

pothesis advanced by Trapp and Weisman (2003) that the strongest surface damage occurs in close association with mesoscale circulations/mesovortices that develop along the outflow boundary. Another maximum in vorticity can be seen to the north and within the black box in Fig. 12. This region of cyclonic vorticity is being produced by a developing mesovortex. Indeed, a small rotational couplet can be identified along the outflow boundary (highlighted by the red arrow in Fig. 12b).

A vertical cross section through the developing apex at this time (Fig. 13) reveals a pronounced change in the kinematic structure compared with the earlier time. The outflow winds are now ~4 km in depth. The component of flow in the plane of the cross section is also stronger (Fig. 13b), suggesting that the rear inflow is intensifying. The region of positive vertical velocities has increased and there has also been a dramatic increase in the updraft magnitude, which is >16 m s^{-1}. The vertical vorticity along the outflow boundary has increased to $>6 \times 10^{-3}$ s^{-1} (Fig. 13a).

4) 0538:00–0548:26 UTC

The third pass by the Omaha bow echo represents the time when the damage rated >F1 was occurring in western Iowa. There is a convex shape to the convective line (~80 km in length) with the apex of the bow echo located in the black box in Fig. 14. The mesovortex has increased in intensity and is now associated with vertical vorticity $>8 \times 10^{-3}$ s^{-1} and is located on the northern edge of the F1 contour. A feature that resembles a hook echo has developed at the apex and is collocated with the mesovortex. This represents clear evidence that a relationship exists between the strongest surface damage and mesovortices. Note that the single-Doppler velocity plot, once again, is not a good proxy for identifying the regions that would be subject to the strongest damaging winds. The largest area of strong, negative Doppler velocities is located in the northern section of the domain; however, this corresponds to an area rated <F0 in damage intensity. This emphasizes the importance of comparing the damage survey with

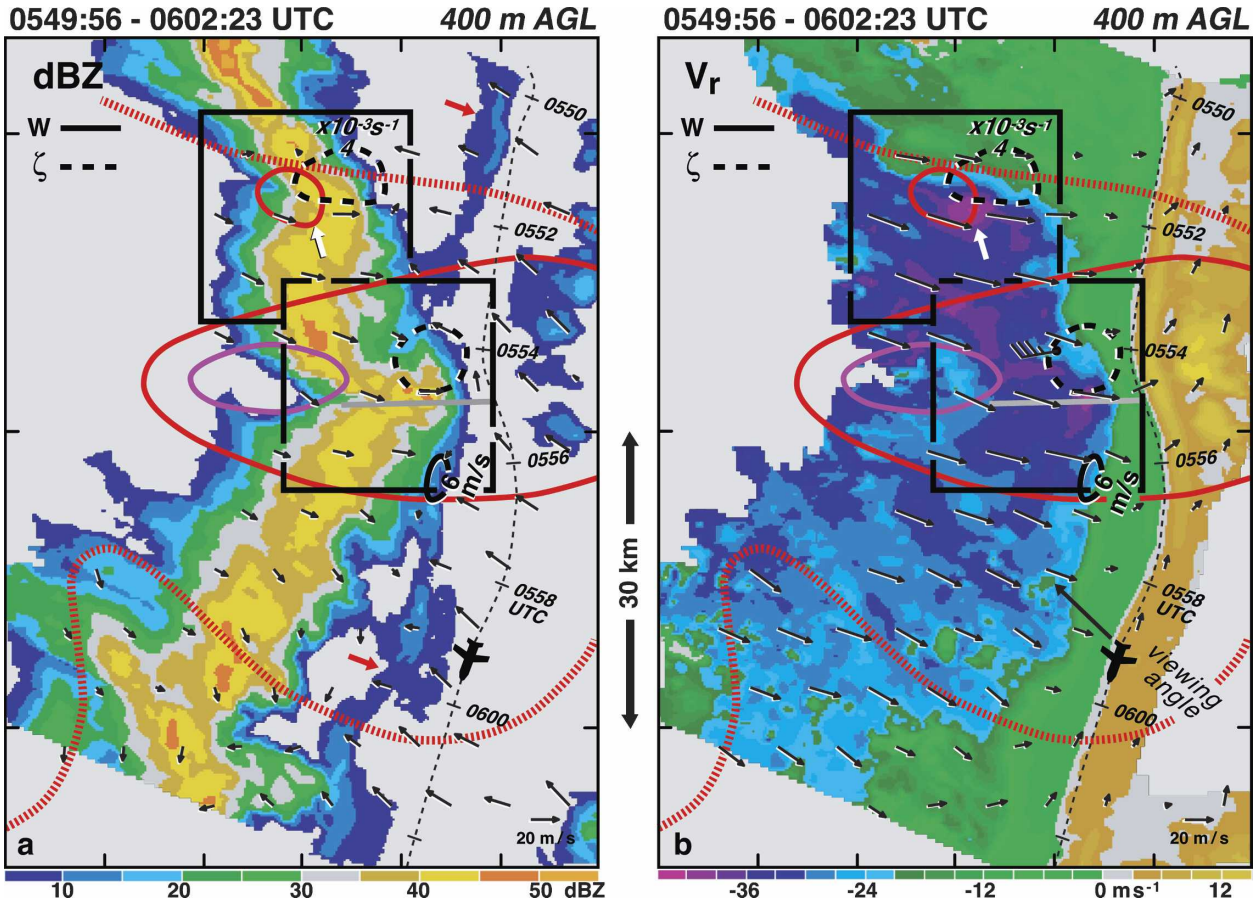

FIG. 15. Same as Fig. 10, but for 0549:56–0602:23 UTC at 400 m AGL. Surface wind report from HNR is shown on the single-Doppler velocity plot. The northern and southern black boxes are enlarged in Part II. The red arrows indicate the position of the thin line associated with the gust front. The white arrow indicates the position of a small bowing segment of the convective line located near a microburst. The gray line shows the location of a range–height indicator (RHI) scan presented in Fig. 16.

the Doppler wind synthesis at the lowest grid level to verify the intensity of the winds at the surface. The strong correspondence of vertical vorticity and surface damage suggests that azimuthal shears (or noting velocity couplets in a plot of storm-relative single-Doppler velocities) are a better field to examine rather than noting the locations of the peak ground-relative velocities shown in Fig. 14b. The vertical cross section through the apex (not shown) reveals a continuing trend of the outflow winds to intensify and deepen. The maximum updraft speeds at the apex increased to >20 m s^{-1}.

5) 0549:56–0602:23 AND 0604:26–0614:42 UTC

The distortion in the convective line was even more pronounced by the fourth flight leg (Fig. 15). The apex has assumed a shape that is reminiscent of a spearhead echo—a radar echo with a pointed appendage extending in the direction of echo motion (Fujita and Byers 1977; Fujita 1985). Its appearance is largely a result of the horizontal advection of precipitation by the rotational flow of the vortex. The gust front (indicated by the thin line and highlighted by the red arrows in Fig. 15a) is ahead of the convective line except near the apex of the bow echo. This is consistent with the conceptualization that the line is surging forward in the vicinity of the apex in response to strong rear inflow.

There is another smaller bow-shaped segment of the line near the location of the microburst shown in Fig. 5b (highlighted by the white arrow in Fig. 15). A pocket of strong, negative Doppler velocities is located slightly east of the F0 contour, and a cyclonic vorticity isopleth ($>4 \times 10^{-3}$ s^{-1}) suggests the presence of a mesovortex. The difficulty of flying near the leading edge of a bow echo is well illustrated in Fig. 15. The flight track shows that the aircraft veered away from the apex at ~0554 UTC to avoid penetrating the echo.

A raw vertical scan by ELDORA oriented approxi-

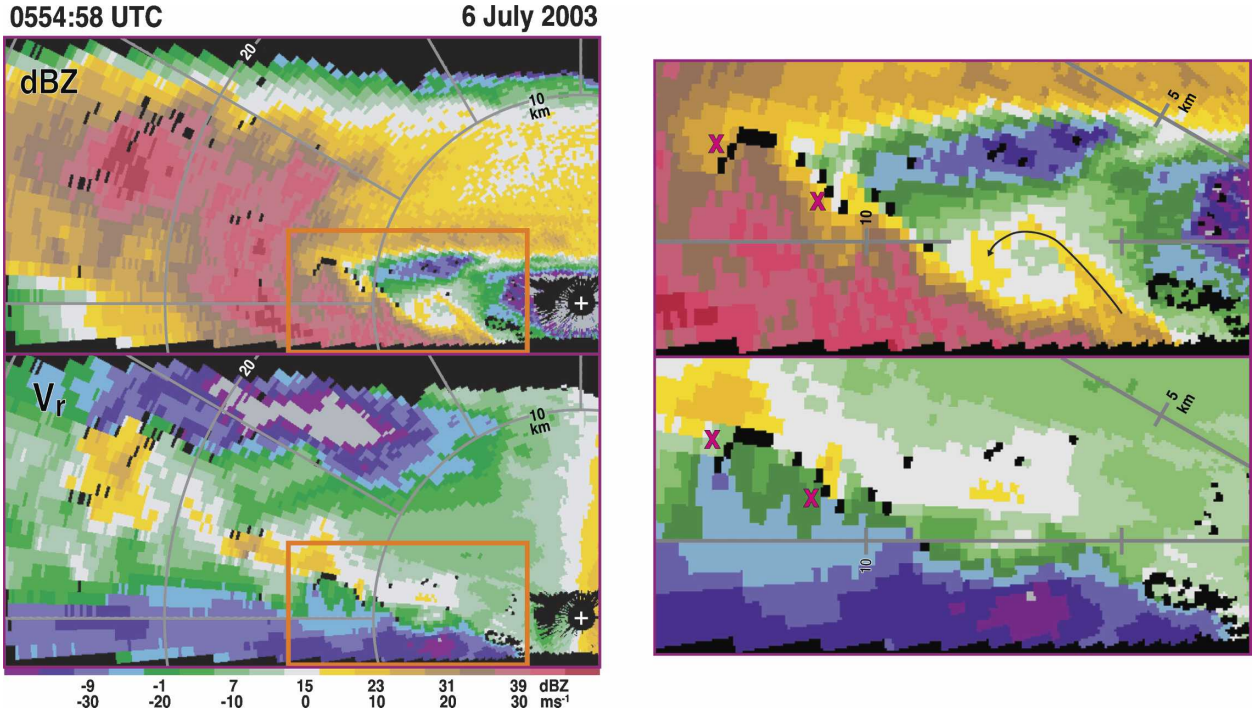

FIG. 16. ELDORA tail radar scan of radar reflectivity and single-Doppler velocities at 0554:58 UTC through the apex of the bow echo. The orange boxes are enlarged on the right. The thin black line on the enlarged radar reflectivity plot denotes the location of a "reflectivity curl" in response to strong shear on top of the outflow. Two rotational couplets are highlighted by the red X on the enlarged plots. The gray lines depict the range and angles from the aircraft. The white cross indicates the position of the aircraft. The location of the scan is shown by the gray line in Fig. 15.

mately west–east through the apex of the bow echo is shown in Fig. 16. Strong, negative velocities (~43 m s^{-1}) are apparent within the outflow, which is several kilometers deep. The storm is tilted upshear in the radar reflectivity image and vast amounts of precipitation are being advected eastward by the outflow winds. It appears that most of the echo return within and at the leading edge of the outflow is from hydrometeors and not from clear-air scatterers (e.g., insects). It is likely that an observer stationed within the storm outflow would have documented sheets of rain moving nearly horizontally.

The enlargements of the radar reflectivity and Doppler velocities on the right-hand side of the figure reveals a pronounced "reflectivity curl" of precipitation (highlighted by the black arrow) within a Kelvin–Helmholtz (KH) billow (e.g., Droegemeier and Wilhelmson 1987; Mueller and Carbone 1987). A similar feature was noted by Wakimoto (1982) and was referred to as a precipitation roll. Additional evidence of circulations produced by KH instability is indicated by the "X"s in Fig. 16. Rotational couplets are apparent at both locations and there are perturbations in the echo pattern that suggest that the precipitation is being displaced by these circulations.

This particular flight leg was unique during the mission because a quad-Doppler analysis between the two airborne radars was possible. The wind synthesis at 1.6 km is shown in Fig. 17. Clearly seen in the storm-relative wind field is a large counterclockwise circulation (70–80 km in diameter). This is the cyclonic member of the bookend vortices shown in Fig. 1 and simulated by Weisman (1993). This system-scale vortex should not be confused with the smaller-scale mesovortex associated with damaging surface winds shown in Fig. 14. The circulation is best defined at midlevels but is evident up to 8 km. The strongest vertical vorticity within the circulation is 5.6×10^{-3} s^{-1} at the 2.8-km level. Other Doppler radar studies that have resolved a vortex of this type include Schmidt and Cotton (1989), Verlinde and Cotton (1990), Scott and Rutledge (1995), and Jorgensen et al. (1997), but none of which during the time that damaging winds were occurring at the surface. The southern branch of this circulation is positioned near the apex. Weisman (1993) has proposed that bookend vortices interact to support a strong rear-inflow current. It is interesting to speculate that this intensifying cyclonic circulation initiated the "bowing process" in the present case. The analysis in Fig. 17 does not extend far enough to the south to fully resolve

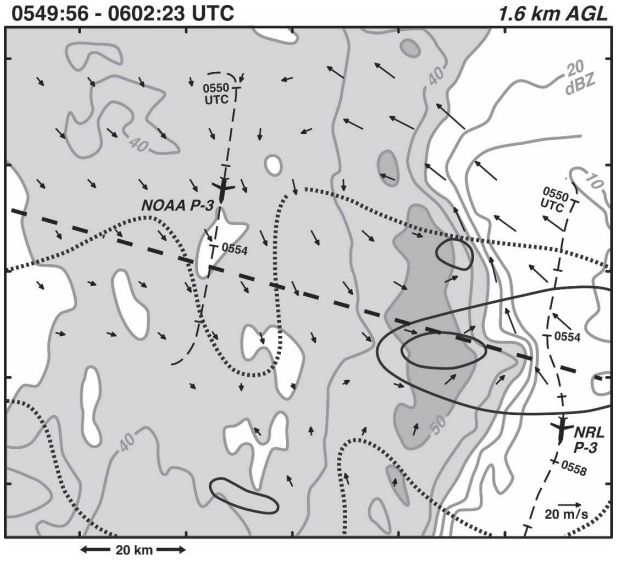

FIG. 17. Multi-Doppler wind synthesis that combines radar data recorded by the NOAA P-3 and NRL P-3 at 0549:56–0602:23 UTC at 1.6 km AGL. Storm-relative winds are plotted. The radar reflectivity is from the WSR-88D located at Omaha. Gray lines are radar reflectivity with values >30 dB*Z* shaded light gray and >50 dBZ shaded dark gray. Thick dashed line represents the location of a cross section shown in Fig. 18. Aircraft tracks are depicted by the thin dashed lines. The damage at the surface is based on the results presented in Fig. 5a and is shown by the dotted and solid black lines.

the anticyclonic vortex. However, anticyclonic turning of the winds at the southern part of the domain suggests that part of the circulation is being sampled.

An approximate west–east cross section through the apex and rear inflow is presented in Fig. 18. The radar reflectivity data from the WSR-88D provides a better depiction of the trailing stratiform region. The ascending front-to-rear flow and descending rear inflow are also apparent in both Figs. 18a and 18b. Indeed, the isopleths of the *u* component of flow in the plane of the cross section shows the descent of the rear-inflow axis from a height centered at 2 km starting ~70 km to the rear of the convective line down to the surface. A more detailed contouring of the isopleths of radar reflectivity (not shown) revealed the position of the "bright band" at ~3.3 km (Fig. 18a).

The final wind synthesis at 0604:26–0614:42 UTC is shown in Fig. 19. The MCS was in its decaying phase at this time as the peak radar reflectivities within the convective line weakened. This is consistent with the position of the gust front (as indicated by the thin line in Fig. 19a), which is located far to the east of the convection, effectively suppressing the warm, moist inflow into the storm system. The superposition of the damage survey analysis on the synthesis suggests that the most intense winds have subsided. The rapid dissipation of the convective line after this time is also supported by the isochrone analysis of the echo structure presented in Fig. 4.

5. Summary and discussion

A detailed analysis of a bow echo that resulted in wind damage over an extensive region (50 km × 200 km) was presented. The maximum damage intensity exceeded F1. The combination of a detailed damage survey with the three-dimensional kinematic structure based on Doppler wind syntheses has not been presented before. Several examples presented in this paper illustrate the ambiguous relationship between the regions of intense single-Doppler velocities at the lowest grid level and the damage reported at the surface.

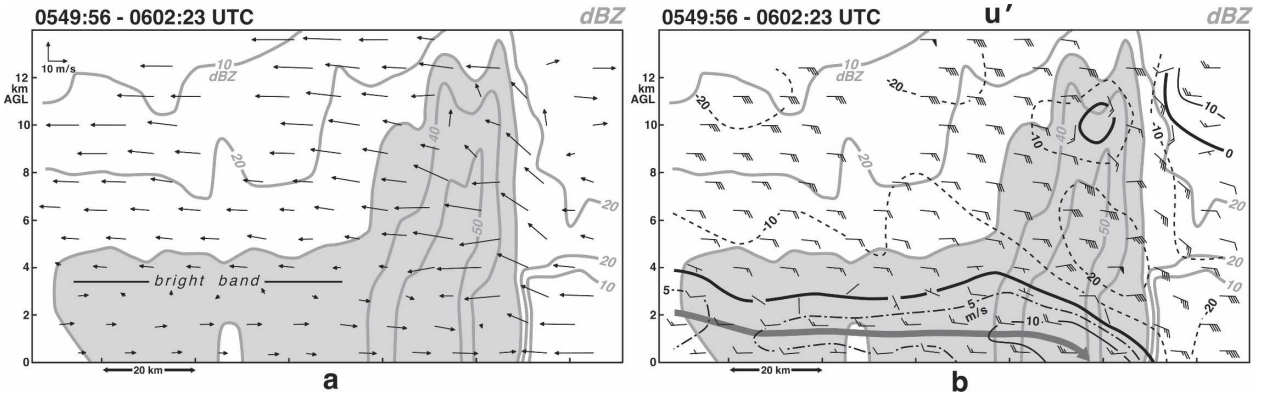

FIG. 18. Vertical cross section through the apex of the bow echo at 0549:56–0602:23 UTC. All plotted fields are storm relative. Radar reflectivity and (a) winds in the plane of the cross section, and (b) *u* component of flow in the rotated plane of the cross section, and storm-relative total horizontal wind vector. Radar reflectivity are plotted as gray lines with values >30 dB*Z* shaded gray. The location of the bright band is shown in (a). The gray arrow in (b) shows the axis of the descending rear inflow. The location of the cross section is shown in Fig. 17.

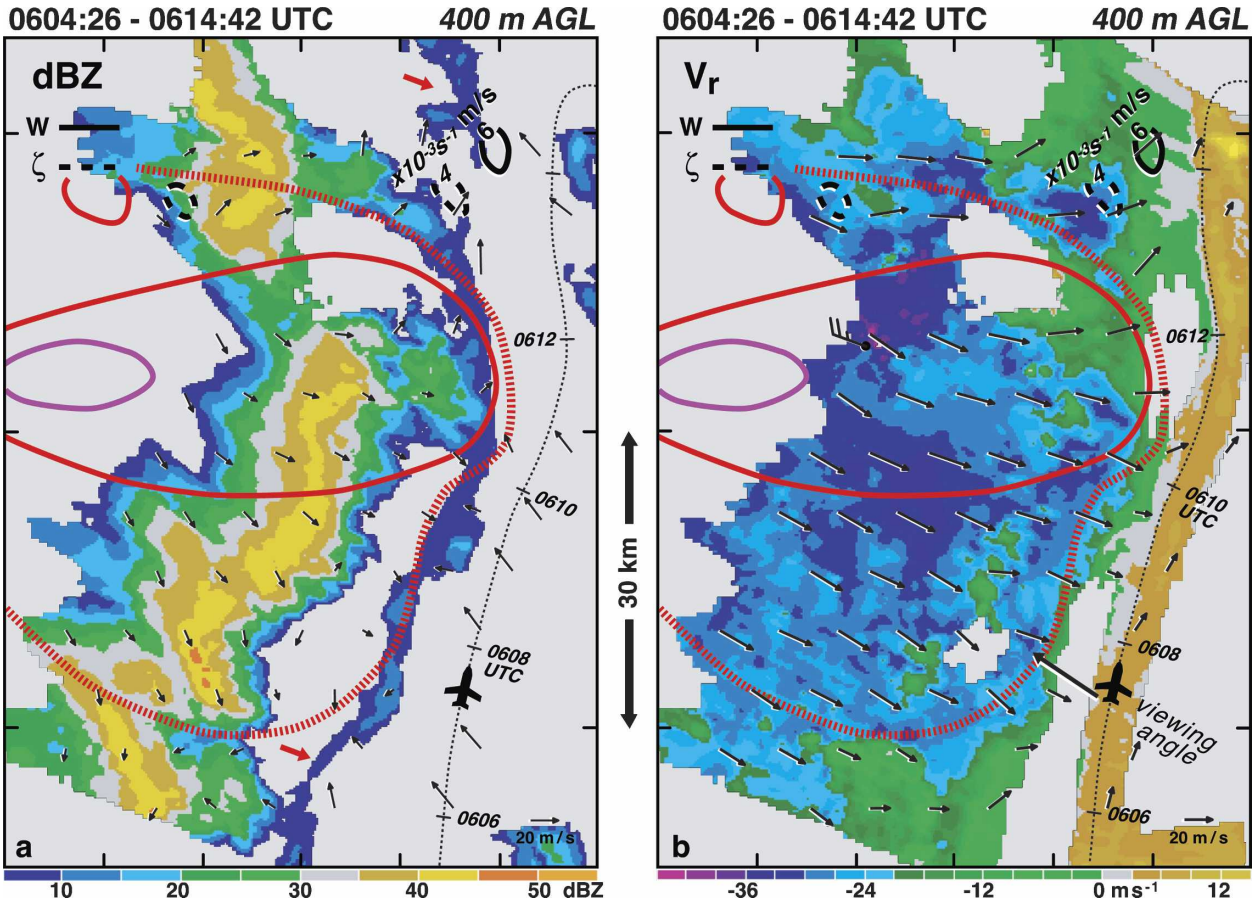

FIG. 19. Same as Fig. 10, except for 0604:26–0614:42 UTC at 400 m AGL. Surface wind report from HNR is shown on the single-Doppler velocity plot. The red arrows indicate the position of the thin line associated with the gust front.

The bowing stage was characterized by both an increase in wind speeds at low levels and a deepening of the outflow winds as revealed in vertical cross sections through the apex. A dramatic increase in the magnitude of the updrafts was also documented. Large amounts of precipitation were advected to the leading edge of the outflow by wind speeds that were 43 m s^{-1}. The vertical wind shear across the top of the cold pool supported the development of KH billows.

A merger between data collected by the two airborne radars during two flight legs permitted an analysis of the bow echo over an extended region. These two analyses appear to capture the incipient and mature stages of the cyclonic bookend vortex. The latter was 70–80 km in diameter at midlevels and was contributing to the rear inflow. It is possible that this enhancement of westerly flow initiated the bowing process.

A hook-shaped echo and mesovortex formed at the bow apex during the time that the most intense damage was occurring at the surface. The center of a strong mesovortex was displaced to the north of the most intense damage. The trend of the strongest surface damage near suspected mesocirculations was shown at several locations along the convective line. The observations may confirm the hypothesis advanced by Trapp and Weisman (2003) suggesting that pockets of intense, straight-line wind damage are associated with mesovortices. Atkins et al. (2005), using single-Doppler velocity measurements, also provide evidence to support this hypothesis. This relationship will be examined in more detail in Wakimoto et al. (2006, hereafter Part II).

Acknowledgments. Research results presented in this paper were supported by the National Science Foundation under Grants ATM-021048 (through RMW) and ATM-0233178 (through NTA).

APPENDIX

Radar Methodology

The ELDORA and NOAA P-3 Doppler data were edited and the aircraft motion was removed from the

velocity field using the Solo II software package (Oye et al. 1995). The data were then corrected for navigational errors using a technique developed by Testud et al. (1995). The along-track data spacing and sweep-angle beam spacing for ELDORA during BAMEX were ~300 m and 1.4°, respectively. The latter led to an effective sampling of ~600 m in the vertical for the distances from the radar used in this study. Accordingly, the ELDORA-only wind syntheses shown in this paper were interpolated onto a grid with a horizontal and vertical grid spacing of 400 and 600 m, respectively. For the analyses that merged ELDORA and NOAA P-3 data (0435–0450 and 0549–0602 UTC flight legs), the interpolation grid was 1.2 km in the horizontal by 600 m in the vertical. The data were time–space adjusted to account for the overall storm motion. The first synthesis used 290° at 21 m s^{-1}. The two subsequent synthesis times used 285° at 22 m s^{-1} during the bowing stage of the MCS. The last three synthesis times used 285° at 20 m s^{-1}. A Cressman filter (Cressman 1959) was applied during the interpolation process with a radius of influence of 400 m in the horizontal and 600 m in the vertical (1200 m in the horizontal and 600 m in the vertical for the combined datasets). Sensitivity studies with larger radii of influence did not significantly alter the results. The lowest level was chosen to be at 400 m AGL.

The synthesis of the radar data was performed using Custom Editing and Display of Reduced Information in Cartesian Space (CEDRIC; Mohr et al. 1986). The intent of this wind synthesis was to provide the general flow features associated with the developing bow echo. Accordingly, a four-step Leise filter (Leise 1982) was applied to the Doppler wind field. This filter effectively removes wavelengths less than 6.4 km. (A three-step Leise filter was applied to the combined datasets, which effectively removes wavelengths less than 9.6 km.) The hydrometeor fall speeds were estimated from the reflectivity terminal fall speed relationship established by Joss and Waldvogel (1970) with a correction for the effects of air density (Foote and du Toit 1969). Vertical velocities were obtained from the horizontal convergence in a variational sense (O'Brien 1970) such that an integration of the anelastic continuity equation met both the upper and lower boundary conditions of $w =$ 0 m s^{-1}. The radar reflectivity from the Omaha WSR-88D was incorporated into the analysis that merged ELDORA and NOAA P-3 data owing to the attenuation problems experienced by both airborne radars.

REFERENCES

Atkins, N. T., J. M. Arnott, R. W. Przybylinski, R. A. Wolf, and B. D. Ketcham, 2004: Vortex structure and evolution within bow echoes. Part I: Single-Doppler and damage analysis of the 29 June 1998 derecho. *Mon. Wea. Rev.,* **132,** 2224–2242.

——, C. S. Bouchard, R. W. Przybylinski, R. J. Trapp, and G. Schmocker, 2005: Damaging surface wind mechanism within the 10 June 2003 Saint Louis bow echo during BAMEX. *Mon. Wea. Rev.,* **133,** 2275–2296.

Burgess, D. W., and B. F. Smull, 1990: Doppler radar observations of a bow echo associated with a long-track severe windstorm. Preprints, *16th Conf. on Severe Local Storms,* Kananaskis Park, AB, Canada, Amer. Meteor. Soc., 203–208.

Chong, M., P. Amayenc, G. Scialom, and J. Testud, 1987: A tropical squall line observed during the COPT 81 experiment in west Africa. Part I: Kinematic structure inferred from dual-Doppler radar data. *Mon. Wea. Rev.,* **115,** 670–694.

Coniglio, M. C., D. J. Stensrud, and M. B. Richman, 2004: An observational study of derecho-producing convective storms. *Wea. Forecasting,* **19,** 320–337.

Cressman, G. P., 1959: An operational objective analysis system. *Mon. Wea. Rev.,* **87,** 367–374.

Davis, C., and Coauthors, 2004: The Bow Echo and MCV Experiment: Observations and opportunities. *Bull. Amer. Meteor. Soc.,* **85,** 1075–1093.

Doswell, C. A., and D. W. Burgess, 1988: On some issues of United States tornado climatology. *Mon. Wea. Rev.,* **116,** 495–501.

Droegemeier, K. K., and R. B. Wilhelmson, 1987: Numerical simulation of thunderstorm outflow dynamics. Part I: Outflow sensitivity experiments and turbulence dynamics. *J. Atmos. Sci.,* **44,** 1180–1210.

Evans, J. S., and C. A. Doswell III, 2001: Examination of derecho environments using proximity soundings. *Wea. Forecasting,* **16,** 329–342.

Foote, G. B., and P. S. du Toit, 1969: Terminal velocity of raindrops aloft. *J. Appl. Meteor.,* **8,** 249–253.

Forbes, G. S., and R. M. Wakimoto, 1983: A concentrated outbreak of tornadoes, downbursts and microbursts, and implications regarding vortex classification. *Mon. Wea. Rev.,* **111,** 220–235.

Fujita, T. T., 1978: Manual of downburst identification for project NIMROD. University of Chicago SMRP Research Paper 156, 104 pp.

——, 1979: Objective, operation, and results of Project NIMROD. Preprints, *11th Conf. on Severe Local Storms,* Kansas City, MO, Amer. Meteor. Soc., 259–266.

——, 1981: Tornadoes and downbursts in the context of generalized planetary scales. *J. Atmos. Sci.,* **38,** 1511–1534.

——, 1985: The downburst. University of Chicago SMRP Research Paper 210, 122 pp.

——, and H. R. Byers, 1977: Spearhead echo and downbursts in the crash of an airliner. *Mon. Wea. Rev.,* **105,** 129–146.

——, and R. M. Wakimoto, 1981: Five scales of airflow associated with a series of downbursts of 16 July 1980. *Mon. Wea. Rev.,* **109,** 1438–1456.

Funk, T. W., K. E. Darmofal, J. D. Kirkpatrick, V. L. DeWald, R. W. Przybylinski, G. K. Schmocker, and Y.-J. Lin, 1999: Storm reflectivity and mesocyclone evolution associated with the 15 April 1994 squall line over Kentucky and southern Indiana. *Wea. Forecasting,* **14,** 976–993.

Hamilton, R. E., 1970: Use of detailed intensity radar data in mesoscale surface analysis of the 4 July 1969 storm in Ohio. Preprints, *14th Conf. on Radar Meteorology,* Tucson AZ, Amer. Meteor. Soc., 339–342.

Hildebrand, P. H., R. A. Oye, and R. E. Carbone, 1981: X-band vs

C-band aircraft radar: The relative effects of beamwidth and attenuation in severe storm situations. *J. Appl. Meteor.,* **20,** 1353–1361.

——, C. A. Walther, C. L. Frush, J. Testud, and F. Baudin, 1994: The ELDORA/ASTRAIA airborne Doppler weather radar: Goals, design and first field tests. *Proc. IEEE,* **82,** 1873–1890.

——, and Coauthors, 1996: The ELDORA/ASTRAIA airborne Doppler weather radar: High-resolution observations from TOGA COARE. *Bull. Amer. Meteor. Soc.,* **76,** 213–232.

Houze, R. A., 1977: Structure and dynamics of a tropical squall-line system. *Mon. Wea. Rev.,* **105,** 1540–1567.

——, S. A. Rutledge, M. I. Biggerstaff, and B. F. Smull, 1989: Interpretation of Doppler weather radar displays of midlatitude mesoscale convective systems. *Bull. Amer. Meteor. Soc.,* **70,** 608–619.

Johns, R. H., and W. D. Hirt, 1987: Derechoes: Widespread convectively induced windstorms. *Wea. Forecasting,* **2,** 32–49.

Jorgensen, D. P., and B. F. Smull, 1993: Mesovortex circulations seen by airborne Doppler radar within a bow-echo mesoscale convective system. *Bull. Amer. Meteor. Soc.,* **74,** 2146–2157.

——, and T. M. Weckwerth, 2003: Forcing and organization of convective systems. *Radar and Atmospheric Science: A Collection of Essays in Honor of David Atlas*. *Meteor. Monogr.,* No. 52, Amer. Meteor. Soc., 75–113.

——, P. H. Hildebrand, and C. L. Frush, 1983: Feasibility test of an airborne pulse-Doppler meteorological radar. *J. Climate Appl. Meteor.,* **22,** 744–757.

——, T. Matejka, and J. D. DuGranrut, 1996: Multi-beam techniques for deriving wind fields from airborne Doppler radars. *J. Meteor. Atmos. Phys.,* **59,** 83–104.

——, M. L. LeMone, and S. B. Trier, 1997: Structure and evolution of the 22 February 1993 TOGA COARE squall line: Aircraft observations of precipitation, circulation, and surface energy fluxes. *J. Atmos. Sci.,* **54,** 1961–1985.

Joss, J., and D. Waldvogel, 1970: Raindrop size distribution and Doppler velocities. Preprints, *14th Conf. on Radar Meteorology,* Tucson, AZ, Amer. Meteor. Soc., 153–156.

Klimowski, B. A., 1994: Initiation and development of rear inflow within the 28–29 June 1989 North Dakota mesoconvective system. *Mon. Wea. Rev.,* **122,** 765–779.

——, M. R. Hjelmfelt, and M. J. Bunker, 2004: Radar observations of the early evolution of bow echoes. *Wea. Forecasting,* **19,** 727–734.

Lafore, J.-P., and M. W. Moncrieff, 1989: A numerical investigation of the organization and interaction of the convective and stratiform regions of tropical squall lines. *J. Atmos. Sci.,* **46,** 521–544.

Laing, A. G., and J. M. Fritsch, 1997: The global population of mesoscale convective complexes. *Quart. J. Roy. Meteor. Soc.,* **123,** 389–405.

Leise, J. A., 1982: A multidimensional scale-telescoped filter and data extension package. NOAA Tech. Memo. ERL WPL-82, 19 pp.

Lin, X., and R. J. Johnson, 1994: Heat and moisture budgets and circulation characteristics of a frontal squall line. *J. Atmos. Sci.,* **51,** 1661–1681.

Mohr, C. G., L. J. Miller, R. L. Vaughn, and H. W. Frank, 1986: The merger of mesoscale datasets into a common Cartesian format for efficient and systematic analysis. *J. Atmos. Oceanic Technol.,* **3,** 143–161.

Mueller, C. K., and R. E. Carbone, 1987: Dynamics of a thunderstorm outflow. *J. Atmos. Sci.,* **44,** 1879–1898.

NCDC, 2003: *Storm Data.* Vol. 45, No. 7, 478 pp.

Nolen, R. H., 1959: A radar pattern associated with tornadoes. *Bull. Amer. Meteor. Soc.,* **40,** 277–279.

O'Brien, J. J., 1970: Alternative solutions to the classical vertical velocity problem. *J. Appl. Meteor.,* **9,** 197–203.

Oye, R., C. Mueller, and S. Smith, 1995: Software for radar translation, visualization, editing and interpolation. Preprints, *27th Conf. on Radar Meteorology,* Vail, CO, Amer. Meteor. Soc., 359–364.

Przybylinski, R. W., 1995: The bow echo: Observations, numerical simulations, and severe weather detection methods. *Wea. Forecasting,* **10,** 203–218.

Schmidt, J. M., and W. R. Cotton, 1989: A high plains squall line associated with severe surface winds. *J. Atmos. Sci.,* **46,** 281–302.

Scott, J. D., and S. A. Rutledge, 1995: Doppler radar observations of an asymmetric mesoscale convective system and associated vortex couplet. *Mon. Wea. Rev.,* **123,** 3437–3457.

Smull, B. F., and R. A. Houze Jr., 1987: Rear inflow in squall lines with trailing stratiform precipitation. *Mon. Wea. Rev.,* **115,** 2869–2889.

Testud, J., P. H. Hildebrand, and W.-C. Lee, 1995: A procedure to correct airborne Doppler radar data for navigation errors using the echo returned from the earth's surface. *J. Atmos. Oceanic Technol.,* **12,** 800–820.

Trapp, R. J., and M. L. Weisman, 2003: Low-level mesovortices within squall lines and bow echoes. Part II: Their genesis and implications. *Mon. Wea. Rev.,* **131,** 2804–2823.

Verlinde, J., and W. R. Cotton, 1990: A mesoscale vortex couplet observed in the trailing anvil of a multicellular convective complex. *Mon. Wea. Rev.,* **118,** 993–1010.

Wakimoto, R. M., 1982: The life cycle of thunderstorm gust fronts as viewed with Doppler radar and rawinsonde data. *Mon. Wea. Rev.,* **110,** 1060–1082.

——, 2001: Convectively driven high wind events. *Severe Convective Storms, Meteor. Monogr.,* No. 50, Amer. Meteor. Soc., 255–298.

——, W.-C. Lee, H. B. Bluestein, C.-H. Liu, and P. H. Hildebrand, 1996: ELDORA observations during VORTEX 95. *Bull. Amer. Meteor. Soc.,* **77,** 1465–1481.

——, H. V. Murphey, C. A. Davis, and N. T. Atkins, 2006: High winds generated by bow echoes. Part II: The relationship between the mesovortices and damaging straight-line winds. *Mon. Wea. Rev.,* **134,** 2813–2829.

Weisman, M. L., 1992: The role of convectively generated rear-inflow jets in the evolution of long-lived mesoconvective systems. *J. Atmos. Sci.,* **49,** 1826–1847.

——, 1993: The genesis of severe, long-lived bow echoes. *J. Atmos. Sci.,* **50,** 645–670.

——, 2001: Bow echoes: A tribute to T. T. Fujita. *Bull. Amer. Meteor. Soc.,* **82,** 97–116.

——, and R. J. Trapp, 2003: Low-level mesovortices within squall lines and bow echoes. Part I: Overview and sensitivity to environmental vertical wind shear. *Mon. Wea. Rev.,* **131,** 2779–2803.

Wilson, J. W., and W. E. Schreiber, 1986: Initiation of convective storms at radar-observed boundary-layer convergence lines. *Mon. Wea. Rev.,* **114,** 2516–2536.

Zipser, E. J., 1977: Mesoscale and convective-scale downdrafts as distinct components of squall-line structure. *Mon. Wea. Rev.,* **105,** 1568–1589.